DEVELOPMENT AND TESTING OF AN ORGANIC SCINTILLATOR DETECTOR FOR FAST NEUTRON SPECTROMETRY

A Thesis
Presented to
The Academic Faculty

by

George Spencer Mickum

In Partial Fulfillment
of the Requirements for the Degree
Masters of Science in the
School of Mechanical Engineering, Nuclear Engineering Program

Georgia Institute of Technology
May 2013

DEVELOPMENT AND TESTING OF AN ORGANIC SCINTILLATOR DETECTOR FOR FAST NEUTRON SPECTROMETRY

Approved by:

Dr. Nolan E. Hertel, Advisor
School of Mechanical Engineering,
Nuclear Engineering Program
Georgia Institute of Technology

Dr. Chris C-K Wang
School of Mechanical Engineering,
Nuclear Engineering Program
Georgia Institute of Technology

Dr. Benjamin Klein
School of Electrical and Computer Engineering
Georgia Institute of Technology

Date Approved: 3/14/2013

To my grandmother, Anna Schwartz and my grandfather, Murray Schwartz

ACKNOWLEDGEMENTS

I would like to start by thanking my advisor, Dr. Nolan Hertel, whose ability to combine patience, support and encouragement have tremendously assisted me during the development of my thesis and the development of myself. His technical and academic guidance has been invaluable. Special words of thanks are due to my thesis advisors Dr. Chris Wang and Dr. Benjamin Klein for giving their advice and being part of my thesis reading committee. I would also like to thank the Office of Radiological Safety, specifically Nazia Zakir, Gary Spichiger and Christina Tabor for their help setting up my experiments in the high bay.

I must finish by thanking my family. I wish to thank my parents, Julia and Luke Mickum for developing their original styles of parenting that have shaped me into the person I am today. As a child, my grandfather instilled my love of math and science and my continued desire to learn, and I owe my perseverance in my academic career to his direction. I would like to especially thank my grandmother. Through her advice I learned politeness and without her I would never have learned the five P's: Prior Preparation Prevents Poor Performance. I would like to thank my stepfather Troy Fontenote who stepped in to help provide the guidance a growing boy needs. Last but certainly not least, I must thank wife, Megan: if I am the cup, then she is the water that fills the empty space inside.

TABLE OF CONTENTS

	Page
ACKNOWLEDGEMENTS	iv
LIST OF FIGURES	vii
LIST OF EQUATIONS	x
LIST OF SYMBOLS AND ABBREVIATIONS	xi
SUMMARY	xii
CHAPTER	
1 Introduction	1
Current Work and Previous Work	1
Background	2
Neutron Properties	2
Neutron Interactions	3
Organic Scintillators	4
Detection	8
NE-213 and Other Names	8
Detection System	9
Methods to Improve Detection	9
2 Theory	12
Detection Process	12
Kinematics	13
Singlets and Triplets Excitation	16
Mathematical Deconvolution of Data	22
3 Experimental Approach	25

Apparatus: Physical Setup, Detector, Shielding, Electronics 25

Procedure: PSD, Calibration, Data Acquisition, Measurements 28

4 Results 32

Response Function Comparison 32

Tabulated and Graphical Unfolding Results 39

Gamma Rejection Ratio 41

Uncertainty Modeling 41

Unfolded Spectra 42

5 Conclusions 58

6 Future Work 59

APPENDIX A: Response Function Data 60

REFERENCES 73

LIST OF FIGURES

Page

Figure 1: Energy transfer diagram in solvent – solute matrix for liquid scintillators. The migration of solvent molecules between excitation from the beta particle and energy transfer to the fluor is depicted as a dotted line[iv]. 6

Figure 2: Energy transfer diagram in solvent – solute matrix for crystal structure of a crystal scintillator. The rigid crystal lattice restricts energy transfer of solvent molecules, dampening the energy migration. 7

Figure 3: Schematic arrangement of the tube structure for a photomultiplier tube showing typical electron trajectories[v]. 10

Figure 4: The recoil proton energy distribution produced by monoenergetic incident neutrons in a hydrogenous material. 13

Figure 5: Elastic scattering of neutrons incident on protons shown in two frames of reference where Ex is the energy of the neutron or proton before the interaction and Ex' is the energy after interaction. 15

Figure 6: After ionization the excited electron seeks out the lowest stable energy state by de-exciting through energy transfer to the surrounding lattice as phonons or through emission of photons. 17

Figure 7: π-electronic energy levels of an organic molecule. 19

Figure 8: Time dependence of scintillation intensity for organic scintillator[xi]. 21

Figure 9: Paraffin shadow shields with lead bases are shown to remove the direct radiation from the measurement to allow for background subtraction of albedo and skyshine. 26

Figure 10: NIM modules for two NE-213 detectors are installed into a single computer rack shown on the left-hand side. 27

Figure 11: BURLE 8575B photomultiplier tube and decoupled light pipe are installed between the NE-213 detector and the ORTEC 265A Photomultiplier Base Assembly. 28

Figure 12: A simple schematic of the data acquisition system involved in the scintillator detector measurements. 31

Figure 13: A sampling of response curves taken from the UMG software unfolding package. 34

Figure 14: A sampling of response curves taken from the UMG software unfolding package. 35

Figure 15: A sampling of response curves extrapolated from the MCNP – PoliMi code and the associated MPPost post processing package. 36

Figure 16: A sampling of response curves extrapolated from the MCNP – PoliMi code and the associated MPPost post processing package. 37

Figure 17: The Na-22 spectrum is shown along with the background measurement. 39

Figure 18: The Na-22 spectrum peaks are highlighted since the acquired spectrum must be analyzed for calibration. Taking the half height of each peak yields the channel number corresponding to the peak energy. 40

Figure 19: The Na-22 spectrum calibration is shown. 40

Figure 20: Raw measurement data recorded from the organic scintillator irradiated with the AmBe source. 42

Figure 21: The Time-to-Amplitude output shows the discrimination capability between neutrons and gammas from the organic scintillator irradiated with the AmBe source. 43

Figure 22: Raw measurement data recorded with neutron gating and low gain settings from the organic scintillator irradiated with the AmBe source. 44

Figure 23: Raw measurement data recorded with neutron gating and high gain settings from the organic scintillator irradiated with the AmBe source. 44

Figure 24:A combination of the unfolded spectral responses for the high and low gain settings on logarithmic scale showing the resolved peaks below 2 and above 8 MeV. 46

Figure 25: The ISO 8529 Standard of the AmBe neutron spectrum. 47

Figure 26: A comparison of the unfolded spectral response and the first iteration neutron spectrum of a 5-Curie PuBe source using FORIST. 48

Figure 27:A comparison of the unfolded spectral response and the first iteration neutron spectrum of an AmBe source using MCNP-PoliMi. 49

Figure 28: A comparison of the measured spectral response and the best approximation spectrum on logarithmic scale estimated with the response functions for the low gain measurement of the AmBe source. 50

Figure 29: A comparison of the unfolded spectral response and the default spectrum for the low gain measurement of the AmBe source. 51

Figure 30: A comparison of the unfolded spectral response and the default spectrum on logarithmic scale for the low gain measurement of the AmBe source. 52

Figure 31: A comparison of the measured spectral response and the best approximation spectrum estimated with the response functions for the high gain measurement of the AmBe source. 53

Figure 32: A comparison of the measured spectral response and the best approximation spectrum estimated with the response functions on logarithmic scale for the high gain measurement of the AmBe source. 54

Figure 33: A comparison of the unfolded spectral response and the default spectrum for the high gain measurement of the AmBe source. 55

Figure 34: A comparison of the unfolded spectral response and the default spectrum on logarithmic scale for the high gain measurement of the AmBe source. 56

Figure 35: A comparison of the measured spectral response and the best approximation spectrum estimated with the response functions for the low gain measurement of the AmBe source. 57

LIST OF EQUATIONS

Page

Equation 1: Recoil proton energy response for non-relativistic incident neutrons. 14

Equation 2: Transformation equation to convert from center-of-mass coordinate system to laboratory frame. 14

Equation 3: Maximum fractional energy transfer in neutron elastic scattering. 15

Equation 4: The exponential equation describing the intensity of emission decays. 20

Equation 5: First order Fredholm integral equation for reconstruction. 23

Equation 6: Discretized linear matrix solution for reconstruction. 23

Equation 7: Measured light output function for MPPost processing code for proton interactions. 38

Equation 8: Measured light output function for MPPost processing code for carbon interactions. 38

Equation 9: Model of epistemic uncertainty in measurement values. 42

LIST OF SYMBOLS AND ABBREVIATIONS

ADC	Analog to Digital Converter
MCA	Multi-channel Analyzer
MCNP	Monte Carlo Neutral Particle
MeV	Mega Electron Volts
MeVee	Mega Electron Volts Electron Equivalent
NE	Nuclear Enterprises
NIM	Nuclear Instrument Module
PMT	Photomultiplier Tube
PSA	Pulse Shape Analyzer
PTB	Physikalisch-Technische Bundesanstalt
RSEL	Radiological Science and Engineering Laboratory
SCA	Single Channel Analyzer
TAC	Time to Amplitude Converter
T-SCA	Timing Single Channel Analyzer
UMG	Unfolding with Maxed and Gravel
VBA	Visual Basic for Applications
VME	Virtual Machine Environment

SUMMARY

The use of organic scintillators is an established method for the measurement of neutron spectra above several hundred keV. Fast neutrons are detected largely by proton recoils in the scintillator resulting from neutron elastic scattering with hydrogen. This leads to a smeared rectangular pulse-height distribution for monoenergetic neutrons. The recoil proton distribution ranges in energy from zero to the incident neutron energy. In addition, the pulse-height distribution is further complicated by structure due to energy deposition from alpha particle recoils from interactions with carbon as well as carbon recoils themselves. In order to reconstruct the incident neutron spectrum, the pulse-height spectrum has to be deconvoluted (unfolded) using the computed or measured response of the scintillator to monoenergetic neutrons. In addition gamma rays, which are always present when neutrons are present, lead to Compton electron recoils in the scintillator. Fortunately, for certain organic scintillators, the electron recoil events can be separated from the heavier particle recoil events in turn to distinguish gamma-ray induced events from neutron-induced events. This is accomplished by using the risetime of the pulse from the organic scintillator seen in the photomultiplier tube as a decay of light.

In this work, an organic scintillator detection system was assembled which includes neutron-gamma separation capabilities to store the neutron-induced and gamma-induced recoil spectra separately. An unfolding code was implemented to deconvolute the spectra into neutron and gamma energy spectra. In order to verify the performance of the system, a measurement of two reference neutron fields will be performed with the

system, unmoderated Cf-252 and heavy-water moderated Cf-252. After the detection system has been verified, measurements will be made with an AmBe neutron source.

CHAPTER 1

INTRODUCTION

Current Work and Previous Work

In this work, an organic scintillator detection system was assembled which includes neutron-gamma separation capabilities to store the neutron-induced and gamma-induced recoil spectra separately. An unfolding code was implemented to deconvolute the spectra into neutron and gamma energy spectra. In order to verify the performance of the system, a measurement of two reference neutron fields was performed with the system, unmoderated Cf-252 and heavy-water moderated Cf-252. After the detection system was verified, measurements were made with an AmBe neutron source.

The use of organic scintillators is an established method for the measurement of neutron spectra above several hundred keV. Fast neutrons are detected largely by proton recoils in the scintillator which result largely from neutron elastic scattering with hydrogen. This leads to a smeared rectangular pulse-height distribution for monoenergetic neutrons. The recoil proton distribution ranges in energy from zero to the incident neutron energy. In addition, the pulse-height distribution is further complicated by the presence of peaks at higher neutron energies by energy deposition due to alpha particle recoils from interactions with carbon and due to carbon recoils. In order to reconstruct the incident neutron spectrum, the neutron-induced pulse-height spectrum has to be deconvoluted (unfolded) using the computed or measured response of the scintillator to monoenergetic neutrons.

In addition gamma rays, which are always present when neutrons are present, lead to Compton electron recoils in the scintillator. Fortunately, for certain organic scintillators, the electron recoil events can be separated from the heavier particle recoil events which can be used to distinguish gamma-ray induced events from neutron-induced events. This is accomplished by using the risetime of the signal from the organic scintillator.

A novel method was used to generate the response functions necessary for deconvolution of the measured data. MCNP-PoliMi is a Monte Carlo simulation tool developed to simulate the neutron interaction and photon production. It differs from the widely used MCNP code in that each collision is recorded in a single separate output file that can be processed to output pulse height distributions. MCNP-PoliMi was applied to generate detector responses to monoenergetic neutrons for the detector used to gather the experimental data.

The process of experimental measurements was described in detail in order to facilitate reproduction of this work for applications in neutron spectroscopy in mixed field measurements. The result of using MCNP-PoliMi is analyzed for benefits and disadvantages. The deconvoluted specta were compared with the published spectra for the americium-beryllium source neutron energies to support the viability of this process for neutron and gamma discrimination with organic liquid scintillators.

Background

Neutron Properties

Neutrons differ from other types of radiation in that they do not interact with the atomic electrons around the nucleus of every element. Their primary interactions are with the nuclei of the detector media. Since neutrons penetrate the electron cloud, methods

allowing for the detection of neutrons must rely on the full or partial transfer of energy of the incident neutron to the nuclei of the constituent atoms. As a result the neutron can be absorbed and disappear completely, or can recoil with a new energy and direction. Both these types of interactions deposit energy in the target nuclei and may create charged particles in the form of internal conversion or recoil nuclei. Neutrons are detected through neutron nucleus reactions that result in energetic charged particles. The detection of these secondary charged particles is necessary since neutrons are not charged particles and cannot be detected by Coulombic interactions.

Neutron Interactions

Neutrons can interact through two main modalities, scattering and absorption interactions. Concerning absorption, charged particle production may occur from neutron interactions with atomic nuclei. But, the probability that a neutron will interact by one of these interactions decreases rapidly with increasing neutron energy. Neutrons from sources such as decay reactions, nuclear reactors, and accelerators have energies ranging from several hundred keV to a maximum above 25-MeV[i,ii,iii]. However, the importance of scatter events rises with increasing neutron energy.

Scatter events can be used to detect higher energy, or fast, neutrons by elastic scattering with nuclei. Elastic scattering interactions are those for which the kinetic energy of the incident neutron and the kinetic energy of scattered particle and neutron are equal. For fast neutrons, these elastic scatter events can result in the transfer of part of their energy on collision to the recoil nuclei or all of their energy on collision with hydrogen nuclei. The energy deposition of these charged recoil or product particles in the detector material may be used to detect the incident neutrons. By means of elastic scattering in hydrogen, a range of collisions are possible, notably including transfer of the entire incident neutron energy in a single collision. Since only a small fraction of overall energy can be

transferred in collision with heavy nuclei, fast neutron detectors are largely based on low atomic number elements especially hydrogenous materials.

Organic Scintillators

Organic scintillators are relied on as a means of detecting fast neutrons because of their high hydrogen content. A scintillator's primary property is the emission of fluorescent light produced by incident ionizing particles on a scale that is detectable. This process is dependent on the excitation and subsequent deexcitation of valence electrons in the scintillating material. As valence electrons interact with the ionizing particle, they become excited and can transition to the conduction band of the material, leaving behind a hole in their electron orbit. These electrons can transition down from their excited state and re-occupy their empty states. When the electron-hole recombination results in photon emission, the electromagnetic wave traverses the medium, propagating in all directions. Upon arriving at the boundary of the scintillator material, this isotropic light can be detected via photomultiplier tubes, electronic counters, or if the light intensity is great enough and between 400 – 700 nm wavelength, visual observation.

Fast neutrons interacting in the organic scintillating material produce recoil protons from elastic scattering reactions with the hydrogen nuclei. The recoil protons serve as the ionizing radiation, depositing their energy over tens of micrometers, shown in Table 1 in Appendix A. Because of low density (<1 g/cc) and low atomic number of constituent elements, organic scintillators have much lower gamma ray absorption coefficients than inorganic scintillators, such as NaI(Tl). Because of this, organic scintillators should provide a good means of distinguishing from gamma-ray events when detecting fast neutrons. The photoelectric absorption is small when the energy is greater than 30 keV and the Compton scattering becomes the main absorption process up to E=2 MeV. Above 2 MeV, pair production becomes appreciable[iv].

The wide use of organic scintillator neutron detectors has led to many different commercially available detectors for specific applications. The many uses include gamma and neutron spectroscopy, dosimetry, fast counting, thermal neutron detection and others. The primary application of organic scintillators is in very fast and ultrafast timing, especially under mixed radiation fields which would paralyze a slower detector. In most organic scintillators the lifetime of a prompt fluorescence lasts only on the order of a few nanoseconds, providing detection under intense radiation bombardment. However because of their susceptibility to gamma ray interactions, the concern is that organic scintillators produce false positives for neutron counts. Even so, because of their lack of molecular architecture, liquid organic scintillators are twice as useful in this scenario since they are intrinsically radiation hardened.

Plastic and crystal organic scintillators both have higher quantum efficiency than liquids, so they have an appreciable component of radiative transfer. However, the solvent – solute transfer is usually less efficient in plastic scintillators than liquids. Since the solvent is rigid, no molecular diffusion occurs, and energy migration is less efficient. This difference can be seen below in Fig. 1 and Fig. 2. The solute is a fluor.

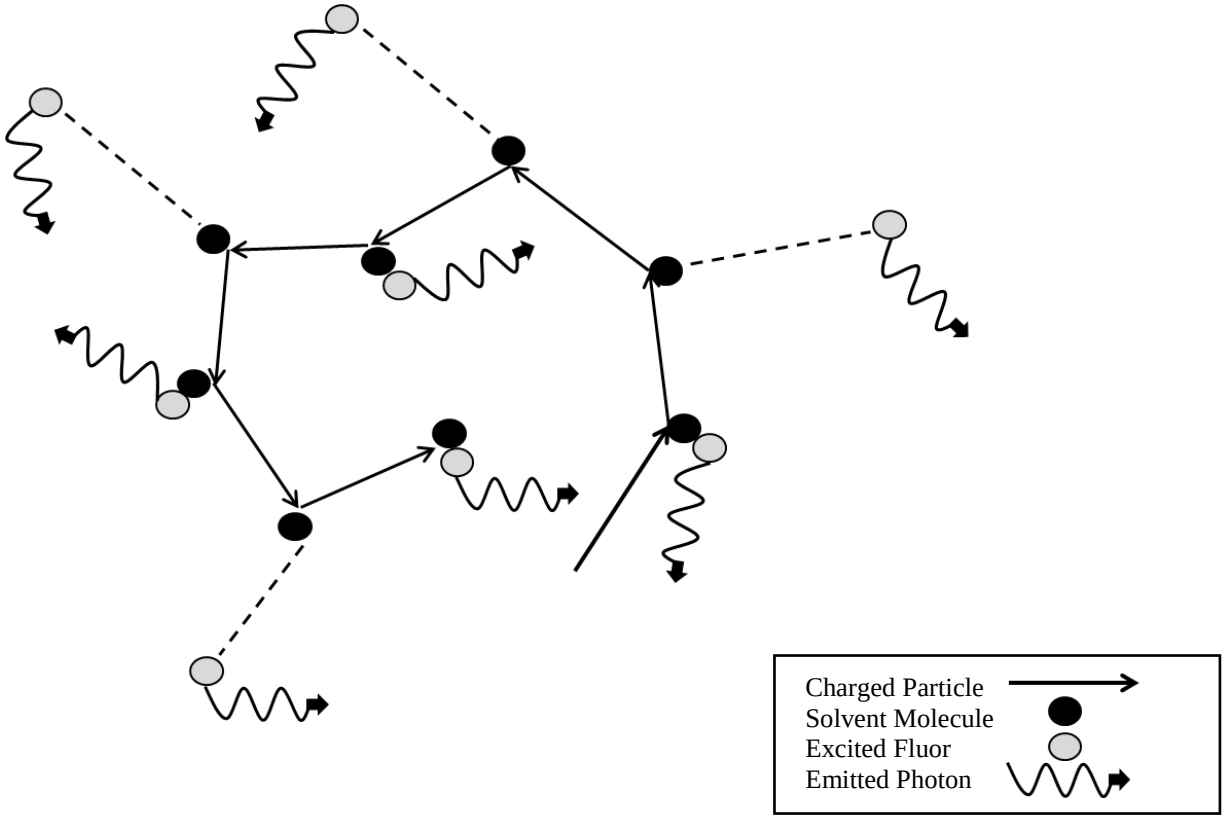

Figure 1. Energy transfer diagram in solvent – solute matrix for liquid scintillators. The migration of solvent molecules between excitation from the beta particle and energy transfer to the fluor is depicted as a dotted line[iv].

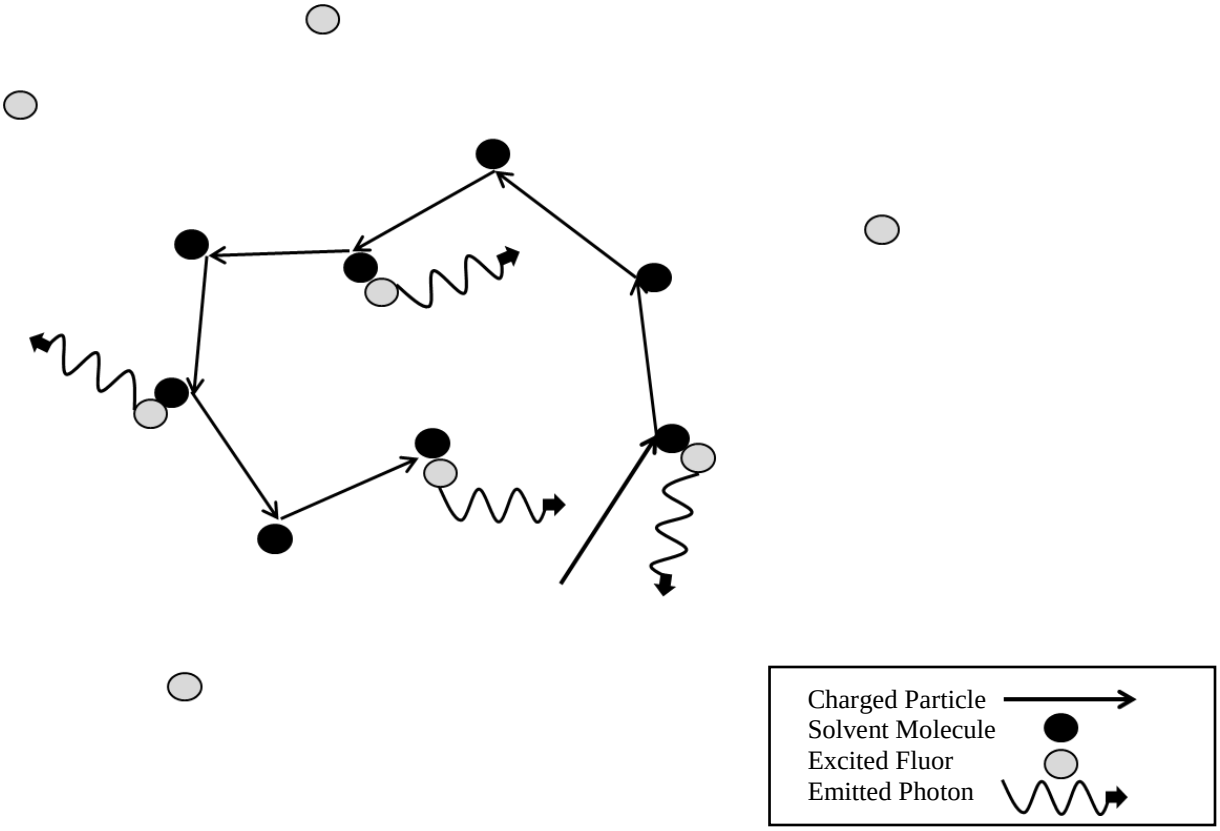

Figure 2. Energy transfer diagram in solvent – solute matrix for crystal structure of a crystal scintillator. The rigid crystal lattice restricts energy transfer of solvent molecules, dampening the energy migration.

Liquid organic scintillators fast response and low Z-value constituents make them preferred for beta and fast neutron detection. In high radiation environments their lack of a rigid crystal lattice and ultra-fast response time makes them useful to separate neutrons and gamma rays. The properties of organic media used as scintillators such that they provide a good means of fast neutron detection are as follows:

1. The media should have high hydrogen content, with a hydrogen/carbon ratio generally greater than one.
2. They should have a high light output, comparable to at least 50 percent of the light output from the organic crystal anthracene.

3. Their wavelength of max emission should be detectable by modern methods, in the range of the visible and ultra-violet wavelength spectral response (100 – 1000 nanometers). Typical response range between 300-500 nm.
4. The medium should be transparent to the wavelength of its own emission, or include wavelength shifters to minimize the optical absorption.
5. The organic scintillator should have a linear response between the amount of energy deposited by the incident radiation and the output light intensity.
6. The risetime of the scintillator should be notably different for each type of radiation and be short to enable fast signal pulse generation.

Detection

NE-213 and Other Names

The Nuclear Enterprises (NE)-213 liquid organic scintillators primary uses are fast neutron spectroscopy and gamma detection in the energy range greater than 100 keV. Popular because of its excellent pulse shape discrimination, the NE-213 performance separates neutron and gamma radiation by the discrimination of the intensity of light created in response to different charged particles. This performance declines as neutron energy drops, since the energy transferred from a slow neutron to the detector material is very low, and thus cannot be detected. As the energy rises, the energy deposited can become noticeable, once reaching the keV range.

The popularity of this detector type has led to other companies creating their own versions, or in the case of Nuclear Enterprises, companies being bought out by new owners. Thus the NE-213 detector has come to be also referred to as the BC-501A or the EJ-301, manufactured by Saint-Gobain Crystals and Eljen Technology, respectively.

Detection System

For this work, the NE-213 organic scintillator was paired with a two inch diameter BURLE 8575B photomultiplier tube (PMT) to convert the light pulses into electronic signal. A voltage pulse collected at the anode of the PMT is linearly related to the scintillation light pulse. The weak light flashes from a scintillator pulse are made detectable by the conversion of light to electrons and the subsequent electron multiplier section in the PMT, shown in Fig. 3. The current signal from the anode was then passed through a pulse shape analysis system composed of several Nuclear Instrumentation Module (NIM) modules and then routed to a multi-channel analyzer (MCA). The analog pulses were digitized by the MCA and displayed on a computer using the ORTEC MAESTRO software package.

Methods to Improve Detection

Small scintillators are preferred to large ones since light transmission in crystals or containers of larger size yield nonuniform light collection efficiency from increased reflection conditions. This can lead to a decrease in detection efficiency since the overall detection area is reduced. But often this effect is mitigated by the increased resolution from better light collection over the detector volume.

Energy resolution is not as important as timing resolution when it comes to pulse shape discrimination. For appropriate neutron gamma discrimination to be possible, the exponential tail of the light intensity decay must be successfully transmitted. This can be accomplished by first of all taking the signal from the anode of the photomultiplier tube. The anode signal is the primary signal analyzed since the typical scintillation pulse has passed through the electron multiplier section to reach the anode, serving to amplify the small tail. The tail of the pulse is important since it is holding the information on particle type, as described in the Detection Process section in the next chapter. A large impedance

in the coaxial cable used to transmit the signal helps retain the signal strength for small currents, especially with long lengths of cable. Furthermore, the amplifier should have low noise characteristics and be operated at low gain for the best time resolution.

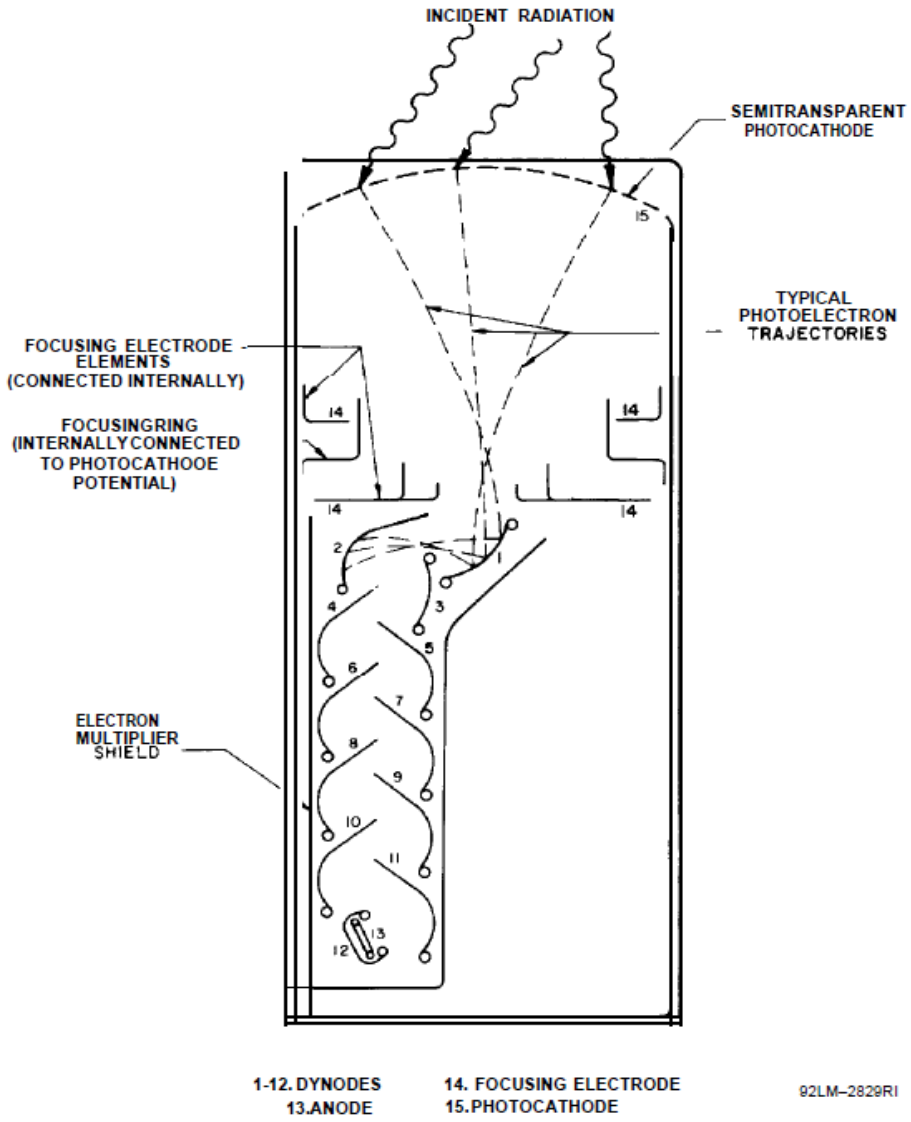

Figure 3. Schematic arrangement of the tube structure for a photomultiplier tube showing typical electron trajectories[v].

The pulse-height distribution is complicated by the presence of peaks at higher neutron energies by energy deposition due to alpha particle recoils from interactions with carbon

and due to carbon recoils. In order to reconstruct the incident neutron spectrum, the neutron-induced pulse-height spectrum has to be deconvoluted (unfolded) using the computed or measured response of the scintillator to monoenergetic neutrons. This unfolding technique in combination with the pulse shape discrimination characteristics of the NE-213 detector allow for a meaningful solution to be obtained from the measurement data.

CHAPTER 2

THEORY

Detection Process

The elastic scattering reaction of neutrons by light nuclei is the most common method of neutron detection in organic scintillators. Light is created when the recoil particles deposit their energy through Coulombic interactions with the electrons in the detector media. Recoil methods are preferred to be used with pulse shape or rise time discrimination to separate neutron events in a neutron-gamma radiation field. Gamma rays, which are always present when neutrons are present, are largely detected via Compton electron recoilsin organic scintillators. For the organic scintillators under consideration here, the electron recoil events can be separated from the heavier particle recoil events and used to distinguish gamma-ray induced events from neutron-induced events.

The scintillation response is markedly different for electrons, protons, or alpha particles each with the same incident energy and thus the neutron pulses can be separated out of the measurement data. The detection process is further complicated by interactions with carbon nuclei. In order to reconstruct the incident neutron spectrum, the neutron-induced pulse-height spectrum has to be deconvoluted (unfolded) using the computed or measured response of the scintillator to monoenergetic neutrons.

Kinematics

The use of organic scintillators is an established method for the measurement of neutron spectra above several hundred keV[vi,vii,viii]. Fast neutrons are detected largely by proton recoils in the scintillator which result largely from neutron elastic scattering with hydrogen. A neutron can lose anywhere from none to its full energy in elastic scattering with hydrogen. The recoil proton distribution then ranges in energy from zero to the incident neutron energy. When coupled with statistical effects, this leads to a version of the rectangular pulse-height distribution for recoil protons from monoenergetic neutrons, as shown in Fig. 4.

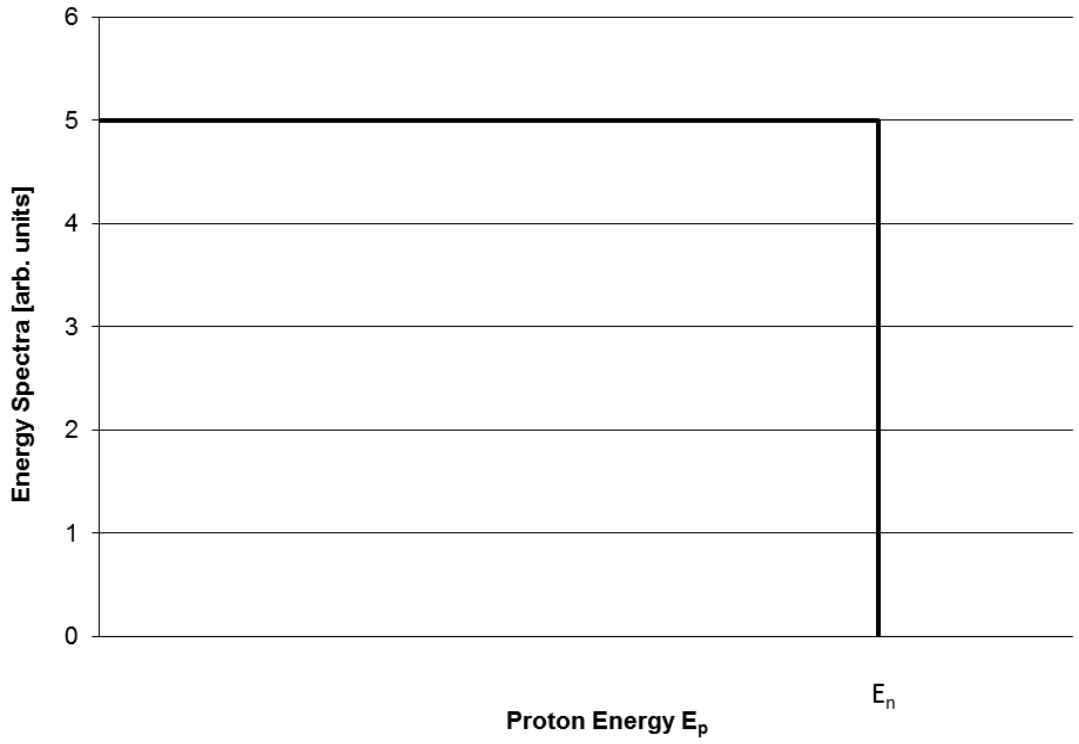

Figure 4. The analytical recoil proton energy distribution produced by monoenergetic incident neutrons in a hydrogenous material.

The recoil proton distribution ranges in energy from zero to the incident neutron energy. For non-relativistic neutrons incident on the organic scintillator the recoil proton response is given by

$$E_p = \frac{2A}{(1+A)^2}(1 - \cos\varphi)E_n \qquad \text{Equation 1}$$

where A is the mass of the proton equal to one, E_n is the energy of the incident neutron, E_p is the recoil proton kinetic energy, and φ is the scattering angle of the neutron in the center of mass coordinate system. Conversion from the center of mass system to the laboratory frame is accomplished using the following transformation

$$\cos\theta = \sqrt{\frac{1-\cos\varphi}{2}} \qquad \text{Equation 2}$$

where θ is the laboratory frame angle between the path of the recoil proton and the incoming neutron. This change between frames of reference allows for simplification of the conservation of energy and momentum equations used to equate the before and after components of the interaction, displayed in Fig. 5 below.

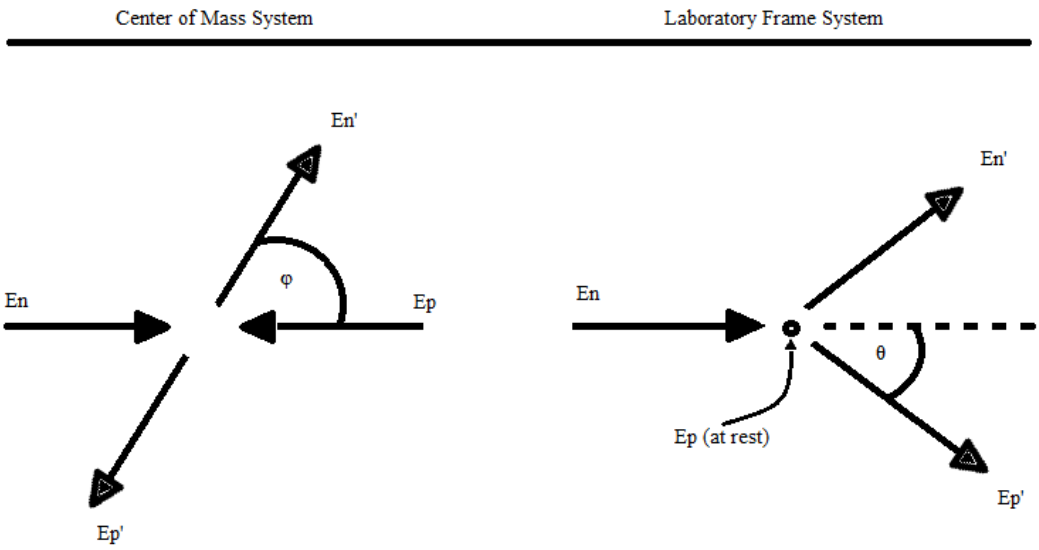

Figure 5. Elastic scattering of neutrons incident on protons shown in two frames of reference where En or Ep is the energy of the neutron or proton before the interaction and En' or Ep' is the energy after interaction.

Combining Equations 1 and 2 forms the relation governing neutron and proton interactions in terms of the recoil angle of the proton. Since the properties of the proton after the scattering are of importance with respect to the incoming neutron the ratio *M* can be used to visualize the maximum fractional energy transfer in neutron elastic scattering for any angle.

$$M = \frac{4A}{(1+A)^2}(\cos\theta)^2 \qquad \text{Equation 3}$$

Using the above relation, the minimum and maximum for *M* are determined when the neutron transfers approximately none of its energy ($\theta \approx 0$) and all of its energy ($\theta \approx 90°$) to the recoil proton. The result of a complete transfer of energy is possible when the recoil is near to perpendicular from the incident path of the neutron. This maximum energy transfer is unique to protons, since as the mass of the target nucleus is increased, the maximum value of *M* is correspondingly reduced. Thus with hydrogen the recoil

proton distribution ranges in energy from zero to the incident neutron energy which leads to a smeared rectangular pulse-height distribution for monoenergetic neutrons.

Singlets and Triplets Excitation

To explain the pulse shape discrimination process, it is necessary to discuss the sequence of processes in the scintillation event in an organic scintillator. The scintillators light output for neutrons has both a fast and delayed components. This may be explained by the excited states of the organic molecules. The shell model of the atom separates the stable energy states of the electronic structure into integer multiples. These energy states defined by quantum theory yield a cascade of discrete energies to ionized electrons such that only specific de-excitation pathways are possible. This can be visualized in Fig. 6. The associated energy that is not radiated between the discrete energy states is expended as heat in the form of phonons. The following section displays the complex π-electron excited singlet and triplet states understood to make a large contribution to the scintillation.

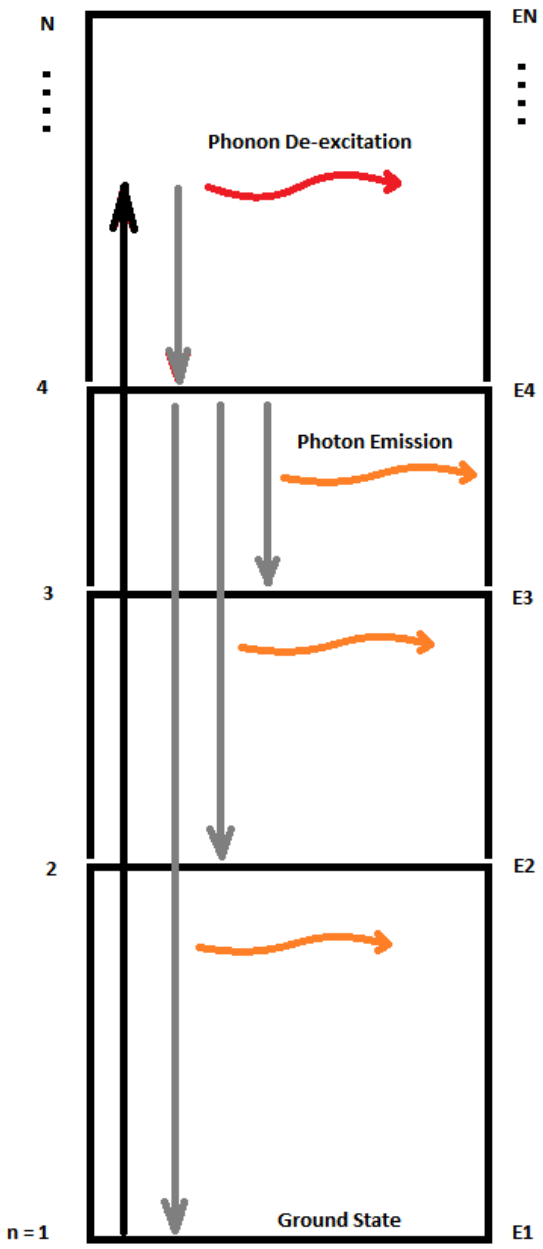

Figure 6. After ionization the excited electron seeks out the lowest stable energy state by de-exciting through energy transfer to the surrounding lattice as phonons or through emission of photons.

An organic molecule is electrically organized into vibrational sublevels between π-electron excited singlet and triplet states. Its utility as a neutron-gamma ray discrimination scintillator is linked with the luminescence properties which can occur as prompt or delayed emission. The photons produced in fluorescence and delayed fluorescence are directly linked with the energy states of the conjugated π-electron systems. Excitation into the π-electron singlet excited states is understood to make a large contribution to the main fast scintillation pulse. Ion recombination into triplet π-states is responsible for the slow scintillation component. This is schematically shown in Fig. 7.

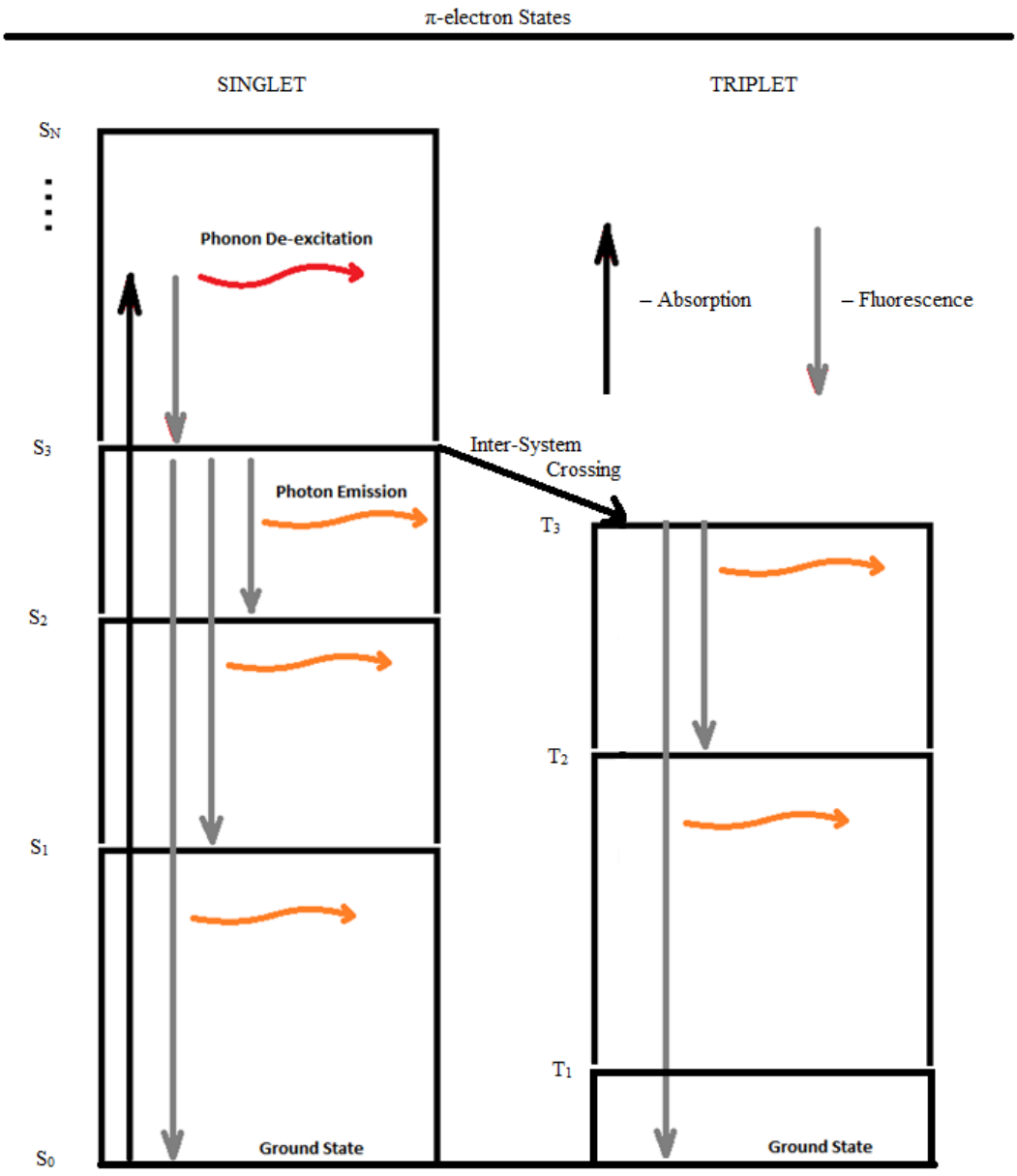

Figure 7. π-electronic energy levels of an organic molecule.

Incident ionizing radiation transfers its energy through Columbic and nuclear interactions to the main constituent of the organic liquid scintillator, the solvent. Either toluene or xylene, two aromatic hydrocarbons, is typically used as the solvent in liquid organic scintillators as well as *p*-terphenyl as the solute and POPOP as the wavelength shifter. A

common feature of a fluorescent organic compound used in scintillator systems is the presence of unsaturated aromatic molecules with conjugated π-electron systems capable of fluorescence. The intensity of the emission decays exponentially according to

$$I = I_o exp(-\frac{t}{\tau})$$ Equation 4

The excitation energy of the solvent is not immediately converted into light. The principal phenomenon associated with the scintillations of organic systems is that the emission spectrum is mainly that of the solute and in the case of ternary systems such as NE-213, the secondary solute. A relatively small fraction of the excitation energy of the solvent being transferred from primary to secondary solute is converted into fluorescence. The prompt or fast decay time of such events is between 2 – 30 nsec. It is known that there is also a slow component of the emission spectra except that decays with a longer decay constant and is spread over the course of several μsec[vi]. It is this slow component that makes particle differentiation using risetimes possible.

Particles produce excitation density and ionization rates within the scintillator volume according to their mass and energy. As the ionizing radiation particle travels through the detector volume, it can deposit energy locally or spread over a large distance. For an incident particle with higher excitation density, from heavier mass or less energy the particle deposits, the scintillation efficiency is reduced from ionization quenching, the mode of decay without emission of a photon. The ionization quenching is much more pronounced in the prompt component of the scintillation light. However, the decay times of the prompt and slow components are not affected. Thus while the light intensity is reduced by ionization quenching, the characteristic exponential decay of the light remains linked to the nature of the incident particle. This link to particle type forms the basis of the technique of pulse shape discrimination. Due to this effect the scintillation response

for electrons, protons, and α particles each of 5 MeV energy, is in the ratio of 10 : 5 : 1 for the energy emitted in the scintillation, respectively[ix].

The scintillation decay curves for three unique forms of radiation is shown in Fig. 8. Fast neutrons produce different decay characteristics from gamma rays and alpha particles due to the intensity of slow components of the light output after an event. Extrapolating on the work with the fast component of Kuchnir and Lynch, the slow components are not only simple exponential, but a combination of at least four components that decay non-exponentially over several microseconds[x,ix]. The effect forms the basis for pulse shape discrimination proposed by Brooks[vi] to distinguish between gamma-ray and neutron-induced events.

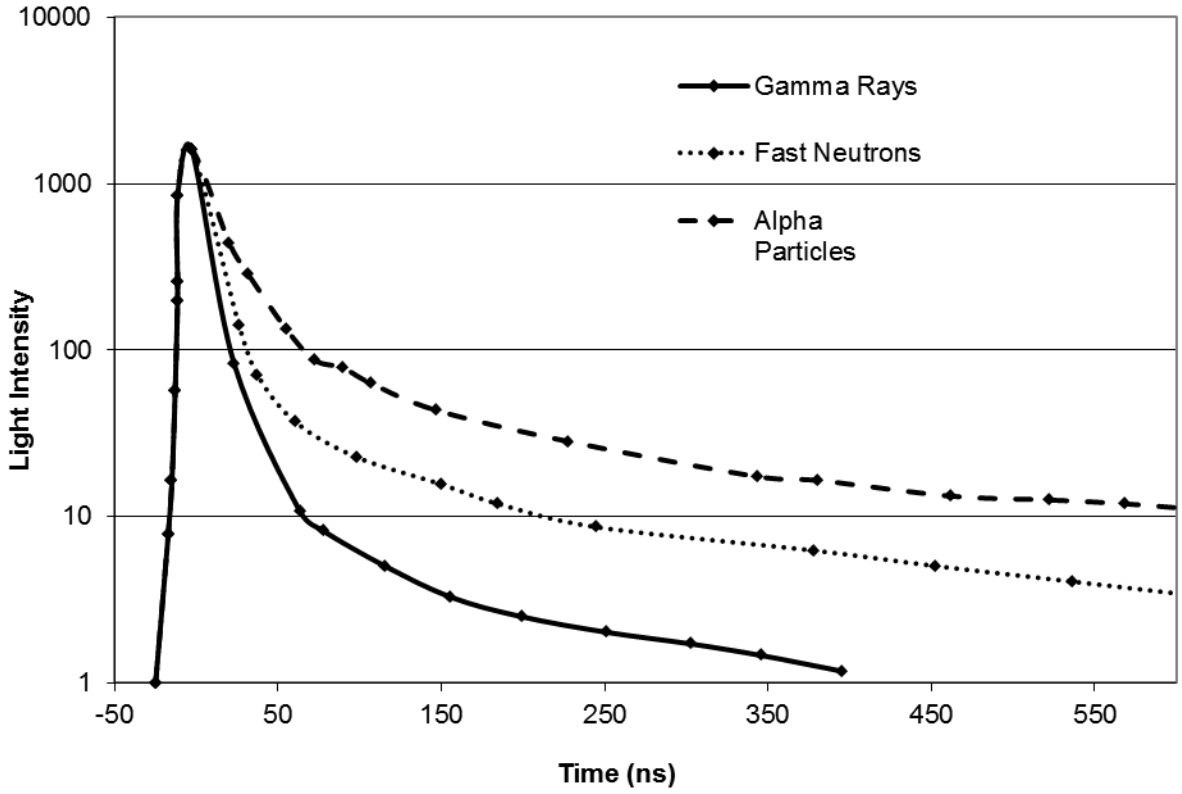

Figure 8. Time dependence of scintillation intensity for organic scintillator[xi].

Mathematical Deconvolution of Data

The use of organic scintillators is an established method for the measurement of neutron spectra above several hundred keV. Fast neutrons are detected principally by proton recoils in the scintillator resulting from neutron elastic scattering with hydrogen. This leads to a smeared rectangular pulse-height distribution for monoenergetic neutrons. The recoil proton energy distribution ranges in energy from zero to the incident neutron energy. The pulse-height distribution is complicated by the presence of structure at higher neutron energies due to alpha particle recoils from carbon interactions as well as carbon recoils due to elastic scattering. In order to reconstruct the incident neutron spectrum, a measured pulse-height spectrum has to be deconvoluted (unfolded) using the computed or measured responses of the scintillator to monoenergetic neutrons, typically in the form of a matrix equation.

Deconvolution is a process primarily involving linear matrix algebra to solve for the spectral fluence. The inputs into the unfolding code are the measured pulse-height spectrum and the detector responses to monoenergetic neutrons. Response functions are obtained computationally or experimentally using monoenergetic neutrons or photons separately. For organic scintillators, the MCNP code has been used to calculate neutron and photon response functions, as has the GEANT code among others[vii,xii]. A first order Fredholm integral equation of the first kind can be evaluated:

$$C_i = \int_0^\infty dE\, R_i(E)\Phi_E(E) \qquad i = 1,2,3,\ldots N \qquad \text{Equation 5}$$

where C_i = count rate for the ith pulse height bin (cps)

$R_i(E)$ = response function for the ith pulse height bin energy E (counts per unit neutron fluence per pulse height bin)

$\Phi_E(E)$ = energy-dependent neutron flux (n/cm^2-sec)

Equation 5 is approximately discretized to the linear matrix solution

$$C_i = \sum_{g=1}^{G} R_{i,g}\Phi_g \qquad i = 1,2,3, \ldots N \qquad \text{Equation 6}$$

where Φ_g= group flux between E_g and E_{g+1} which is the total measure of neutron fluence between the upper bound of energy E_{g+1} and the lower energy bound E_g

$R_{i,g}$ = multigroup form of the i^{th} detector response

Equation 5 and Equation 6 do not have unique solutions, even in the situation where the same number of groups and bins are used, and depending on the approach to minimize the uncertainty, may be over or underdetermined. This is because the continuous function $\Phi_E(E)$ cannot be defined by a finite number of discrete measurements. The number of particle fluence groups is on the same order of magnitude to the number of detector channels for the NE-213 detector. The use of a multichannel pulse-height distribution usually leads to a system of overdetermined systems of equations (number of pulse-height channels is larger than the number of energy groups considered). In systems that yield a few channel responses, e.g. total counts for a small number of detectors, the system is underdetermined and requires an iterative solution. There is also an error in the unfolded response due to statistical and systematic uncertainty. This instability makes the results less reliable, therefore any approach to gathering neutron energy spectra that relies on unfolding measured data will always include inherent error[xiii].

There are a number of computer codes available for solving this system of equations, in particular GRV_MC33 and MXD_MC33[xiv]. GRV_MC33 is a least squared fitting iterative algorithm based on the SAND-II code[xiv]. MXD_MC33 is based on maximum entropy iteration routine and can be traced back to Bayesian theory[xiv]. However, the *a priori* information which separates Bayesian theory from the frequentist methods, or the standard methods used for interpretation of probability, is not necessary. More information is acquired using the multichannel NE-213 detector instead of a few channel

detector since the unfolding since more information is available. Though this inclusion of pre-information simplifies the multichannel approach, a large uncertainty matrix is needed to account for the error in multichannel unfolding, e.g. a multichannel response matrix for 1000 particle energies and 1000 channels i.e. 10^6 elements has to be described by a 10^6 x 10^6 = 10^{12} – element uncertainty matrix[xv].

CHAPTER 3

EXPERIMENTAL APPROACH

Apparatus: Physical Setup, Detector, Shielding, Electronics

The NE-213 detection system was tested at the Radiological Science and Engineering Laboratory (RSEL) facility in the Boggs Building at Georgia Institute of Technology. The neutron sources utilized for measuring detector response were a californium -252 spontaneous neutron source and an americium-beryllium source. Since the measurements used highly radioactive sources, they were performed in a highly shielded room in the RSEL. The dose rate ratio for the AmBe at one foot away inside the room was above 200 mrem/hr and behind the closed door was recorded to be less than 2μ rem/hr. A shadow shield was used to measure the room-returned neutron response, see Fig. 9. This allowed the background response to be removed from the total response to obtain the detector response to radiation coming directly from the source. The sphere shown in the figure is the heavy water moderating sphere with the Cf-252 source inside it.

Figure 9. Paraffin shadow shields with steel bases are used to attenuate all radiation from the measurement and arrive at the background due to room-returned and air scattered neutrons.

A StarTech.com computer rack was used to organize the NIM modules into a single unit for the NE-213 detectors, complete with all the necessary equipment to run two detectors simultaneously. The example setup shown on the left in Fig. 10 is placed next to another StarTech.com rack for comparison.

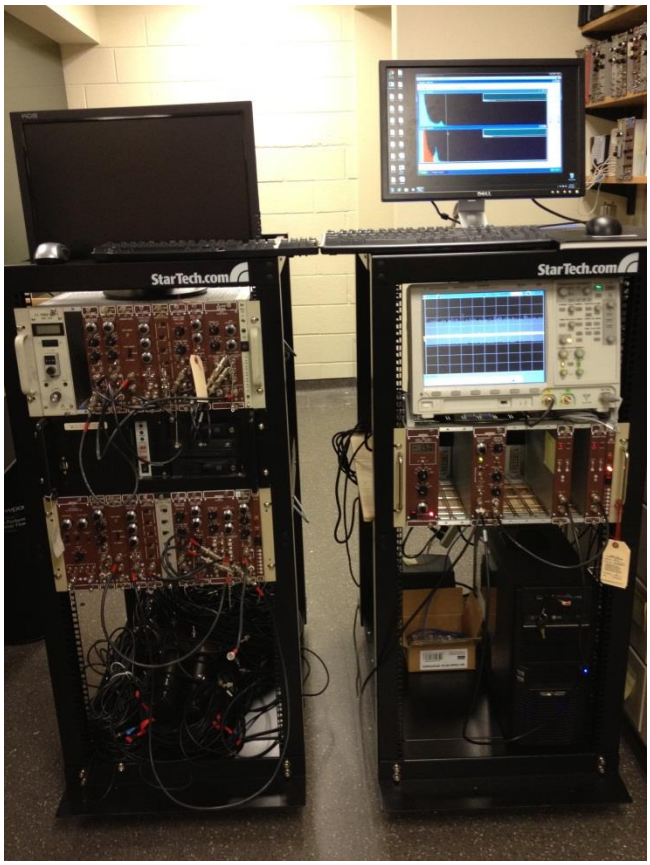

Figure 10. NIM modules for two NE-213 detectors are installed into a single computer rack shown on the left-hand side.

The detector used in this neutron gamma discrimination system has light emission times that depend on the radiation type that induced the scintillation light. Thus neutrons and gammas produce different decay signatures in the NE-213 detector. A BURLE 8575B photomultiplier tube (PMT) was used to collect the light pulses from the NE-213 detector and convert them to a charge pulse. The PMT and detector were coupled together with a ¾" long light pipe with both sides smeared with optical grease for optimal coupling, shown in Fig. 11.

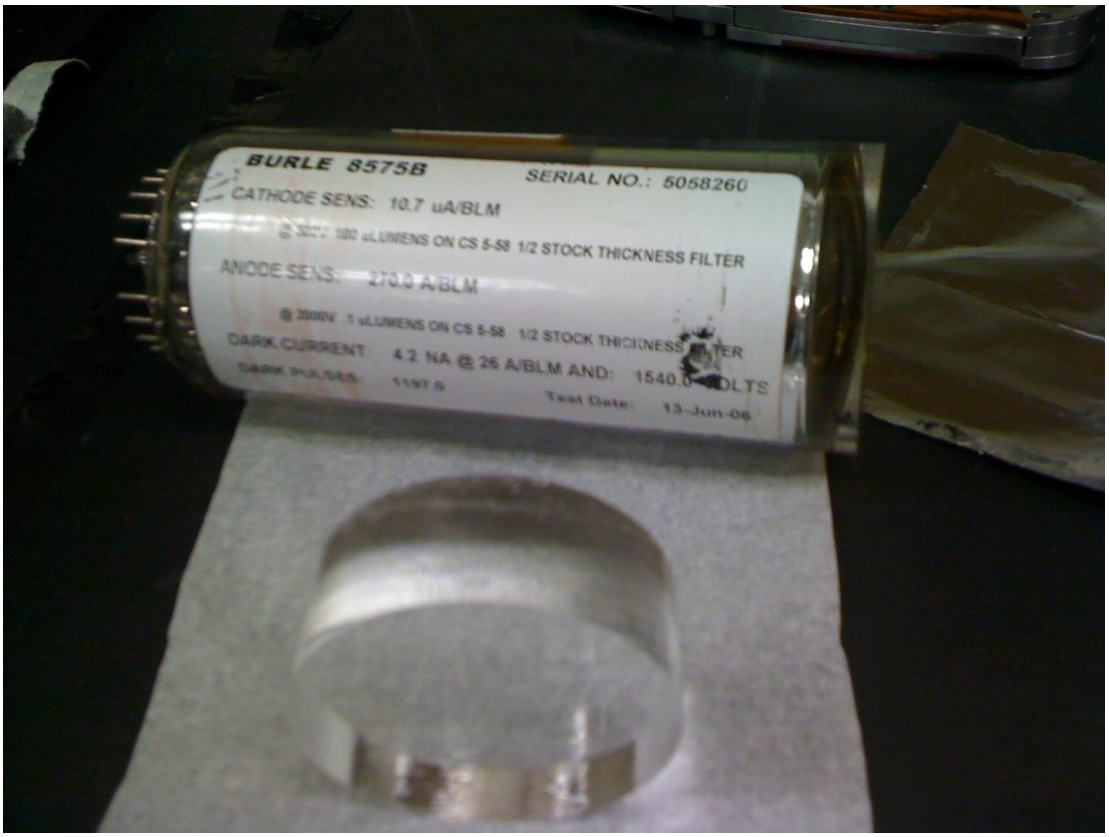

Figure 11. BURLE 8575B photomultiplier tube and the light pipe shown are installed between the NE-213 detector and the ORTEC 265A Photomultiplier Base Assembly.

Procedure: PSD, Calibration, Data Acquisition, Measurements

Initial measurements were done with a californium source to determine the system settings to perform the measurements. Once the detection system was adjusted to distinguish between neutrons and gamma rays, measurements began in the RSEL. The NE-213 detector was oriented so that the radiation from the source was incident on the flat surface of the detector. The expansion chamber seen as the black protrusion in Fig. 9 was situated to remove the bubble from the active detection chamber during measurements. The detector was mounted 46 inches off the ground and 42 inches horizontally from the neutron or gamma source. The principle measurements of interest in this thesis were an unmoderated americium-beryllium neutron source, an unmoderated

californium-252 neutron source, and a heavy-water moderated californium-252 neutron source. Detector calibrations were performed using a sodium-22 gamma ray source and a background measurements withi no source present. Finally, shadow shields were used in the AmBe measurement to remove room-returned and air-scattered radiations from the data acquired without the shadow shield in place.

Calibration of the system was based on measurements with a sodium-22 gamma ray source. This source has two gamma-ray lines: 0.511 MeV annihilation gamma rays since it is a positron emitter and a 1.275 MeV gamma ray. The spectrum acquired with a Na-22 must be using the Compton edges of these gamma rays since this is the prevalent interaction in a low atomic number material. The half height of each peak was chosen to be the channel number corresponding to the Compton edge location. The Na-22 measurement was taken with the discrimination set to obtain the rejection ratio for the gamma ray background. This information was used as a means to see how many gammas were recorded as neutrons within the neutron decay time window.

The high voltage and amplifier controls were set to low gain runs. Additional high gain runs were needed to acquire low energy data. The signal from the NE-213 was routed from the twelfth dynode of the PMT through a pre-amplifier and into a delay line amplifier operated at low gain settings. The delay line amplifier provided delay-line shaping to the pulse before it entered the pulse shape discriminator circuitry. An ORTEC PSA/T-SCA was used for pulse shape discrimination. When this instrument is included in the system, a neutron-gamma discrimination can be effected such that the input signal into the time-to-amplitude converter (TAC) can be used to gate the neutron and gamma spectrum separately. A start and stop signal are picked off the TAC, where the start and stop signal time difference is related to the risetime or pulse shape. Thus the TAC gives the risetime spectra. Shown in the below Fig. 12, the nuclear instruments setup is

depicted in a simplified schematic. NIM modules for the NE-213 detectors include the ORTEC 460 Delay Line Amplifier, ORTEC 552 Pulse Shape Analyzer/Timing Single Channel Analyzer (PSA/T-SCA), ORTEC 567 Time-to-Amplitude Converter/Single Channel Analyzer, and ORTEC 426 Linear Gate. Not shown in the schematic is the ORTEC 427A Delay which enabled the timing of the input signal and the gate signal to be properly correlated and a ORTEC ADCAM MCB for multichannel binning of the pulse-height spectra. Additionally, the PMT signal was input into an ORTEC 113 Preamplifier. An additional ORTEC 572 amplifier was used to separately amplify the energy signal from the PMT to avoid running the signal through the Delay Line Amplifier, however this approach was optional.

The PSA/T-SCA utilized trailing-edge constant-fraction timing to begin the gating process for the PSD circuit. By creating a start and stop signal of the input pulse at ten percent and ninety percent timing fractions of the risetime, the time information related to the light emission is acquired. The PSA/T-SCA provides start and stop signals, both terminated with 100 Ω resistors, are input to the TAC/SCA to measure the time interval between the input pulses. The TAC/SCA output pulse width is equal to the time range from the occurrence of the initial start signal to the end of the stop signal. The TAC output is a voltage proportional to the risetime of the pulse and is used to set the window for neutron events.

By analyzing the TAC output, the lower level discriminator SCA can be adjusted for the precise placement necessary to gate the signal so that only neutron related pulses are allowed to be tallied on the computer. The rise time spectra was input into a multi-channel analyzer using a 2 μsec time range from a selectable range between 50 nsec – 2 msec on the TAC/SCA. Once the TAC discriminator is set, the Linear Gate is included in the pulse discrimination system to reject those pulses with timing characteristics

signifying a gamma pulse. The gated output from the Linear Gate and the original signal from the delay line amplifier were binned in a multi-channel analyzer. A large impedance in the coaxial cable used to transmit the signal helps retain the signal strength, especially with long lengths of cable, thus 93 Ω resistance coaxial cable was used.

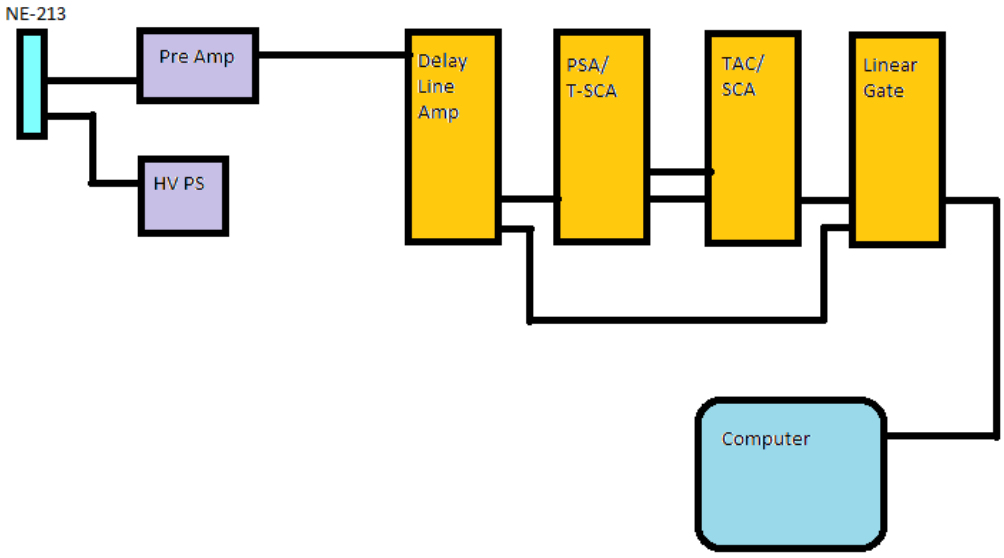

Figure 12. A simple schematic of the data acquisition system involved in the scintillator detector measurements.

The neutron spectra measurements which were performed for this work each were taken over a time period between several hours and several days to minimize counting error. After the counts in the Compton edge or proton recoil region of the measured spectra reach beyond ten thousand, this error becomes negligible. The increased time for the measurements mitigated the effect of any induced error from drift, resulting in lower pulse height resolution.

CHAPTER 4

RESULTS

Response Function Comparison

Initially measurements were analyzed using the response functions provided with the UMG software. The unfolded output spectrum was limited to the energy ranges of the response functions which stopped at 3 MeV thereby missing a large portion of the neutron source spectrum. This difficulty was compounded by the application of detector specific response functions to a unique detector. Monoenergetic neutron detection experiments at Physikalisch-Technische Bundesanstalt (PTB) for a specific NE-213 detector were used to generate the response functions in the UMG software package. The task of experimentally determining response functions for the available detector was outside the scope of this thesis. In the author's opinion, the application of these response functions to any other NE-213 detector would reduce the accuracy of the results. Each NE-213 detector must be coupled with its own unique set of response functions for guaranteeing accurate unfolding results or verify the response functions applied to a new detector with a known neutron source.

Generating response functions was accomplished using the MCNP – PoliMi software. The PoliMi code correlates neutron interaction and photon production so that at each collision relevant information is recorded for further analysis. An associated post-processing code accepts the recorded collision data and applies light output functions to each individual interaction, processing the raw collision data to an output of a pulse height response in matrix form. To accomplish this, several steps were taken:

1. MCNP-PoliMi input files are created modeling the NE-213 detector used for thesis measurements. Mono-energetic neutrons from 300 different energies were modeled between 0.01 MeV and 12 MeV, the flux spectrum energy range expected for the Am-Be source[xvii].
2. The collision information generated by PoliMi is input to the post-processing code for each of the 300 separate energies. The detector type (liquid organic scintillator) is input for the corresponding photon light conversions along with associated number of particles run (in this case nps set to 1 so output is not normalized to the number of particles run).
3. Data output from the post-processing code is transferred to Microsoft Excel and organized into a single response function file for use in UMG.

Examples of each file can be seen in Appendix A. Batch files were utilized to run the 300 PoliMi input energy files and the subsequent post-processing files. Scripts written in Microsoft Visual Basic for Applications (VBA) organized all data outputs and arranged all relevant data into formats consistent with the UMG unfolding code. Microsoft Excel was used to create single MCNP-PoliMi input and post-processing code control files while imbedded Macros iterated on the single files to update them for unique energies from the range of MeV analyzed.

A comparison of the MCNP-PoliMi and UMG response functions became possible after an older set of UMG responses to higher energies above 3 MeV was found. Therefore a comparison of the generated MCNP – PoliMi response functions and those included in the UMG unfolding package was possible. In Fig. 13 – 16 ,some of the response curves for the UMG and MCNP – PoliMi are shown.

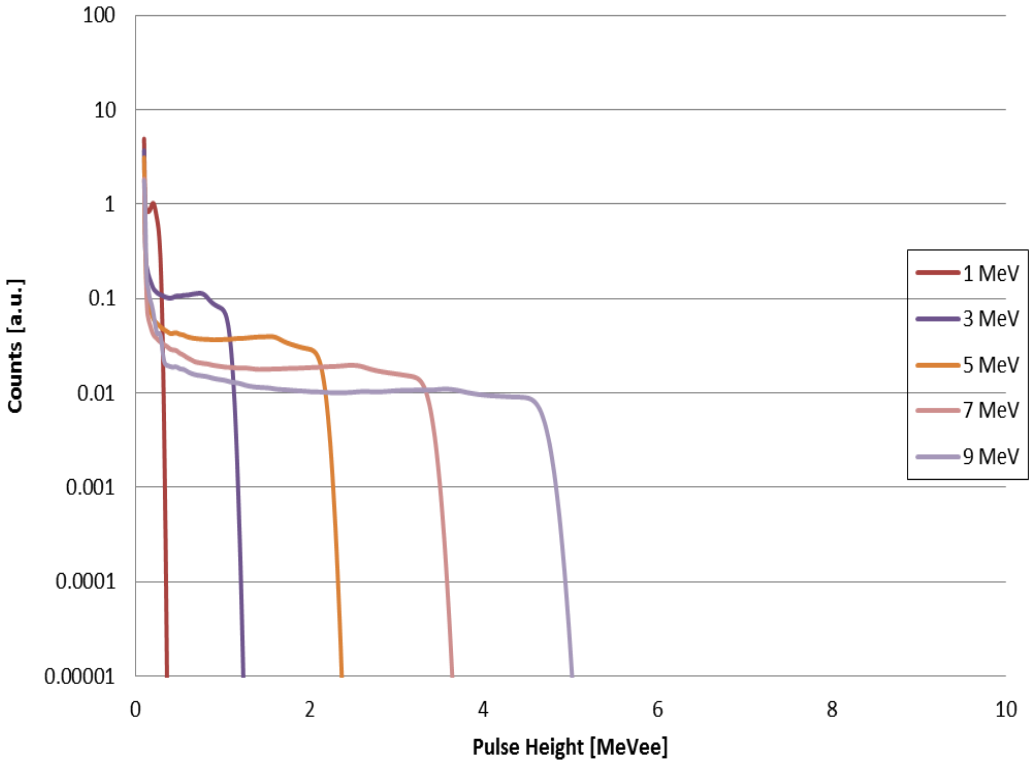

Figure 13. A sampling of response curves taken from the UMG software unfolding package.

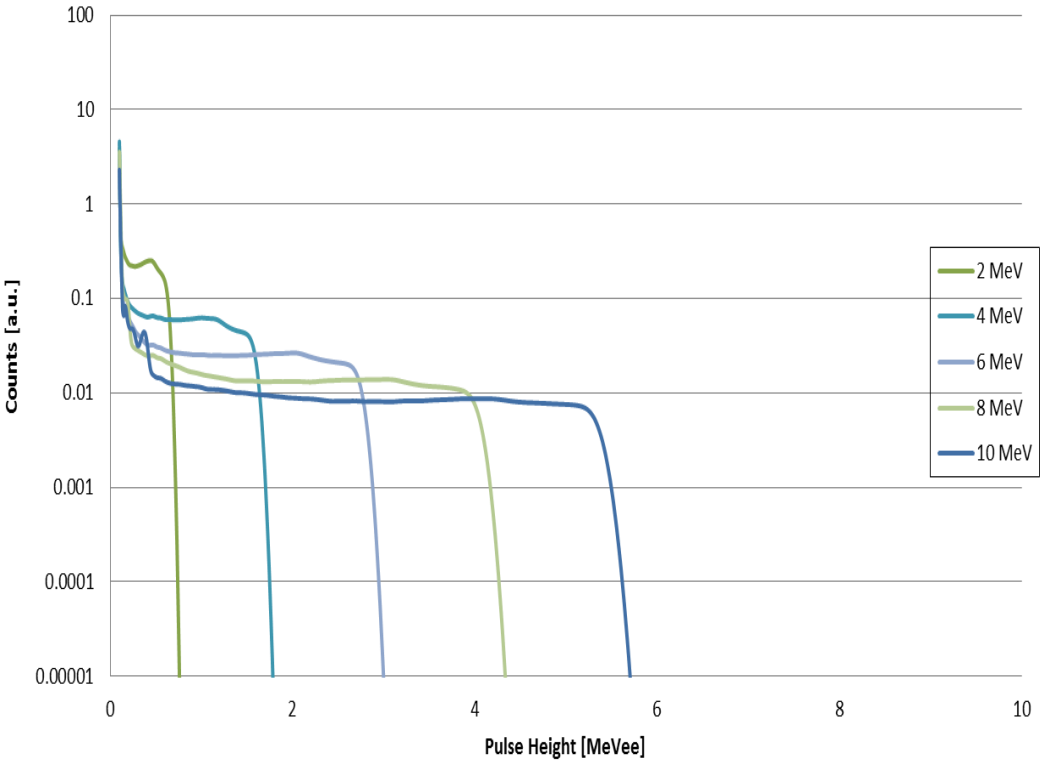

Figure 14. A sampling of response curves taken from the UMG software unfolding package.

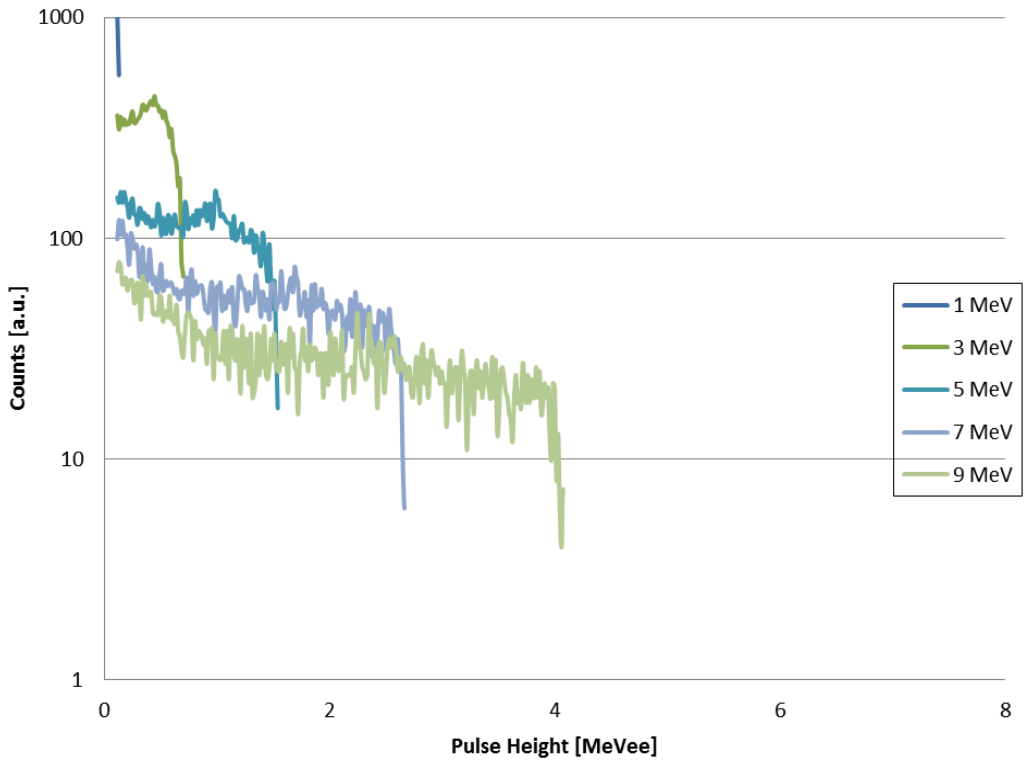

Figure 15. A sampling of response curves extracted from the MCNP – PoliMi code and the associated MPPost post processing package.

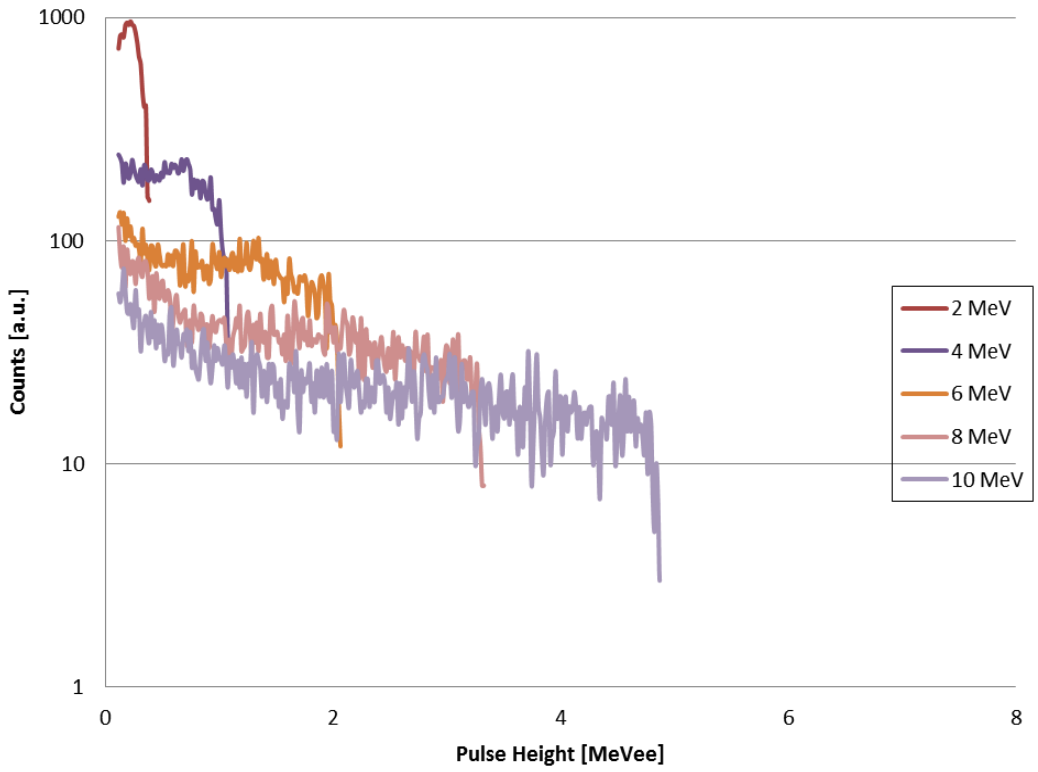

Figure 16. A sampling of response curves extracted from the MCNP – PoliMi code and the associated MPPost post processing package.

The UMG response functions appear to have been smoothed which is a common approach. The UMG unfolding code was implemented to deconvolute the measured spectra into neutron energy spectra using the higher energy UMG responses. An input control file was used to input necessary information into UMG; an example is shown below.

5-10-2012_Cf-252&Bkgd_2inbubble_1000.phs	file with data
RespFunc.rsp	file with response functions (RF)
0.081,10.5258	lo, hi MC E bin edges
0.000, 12.0	lo, hi RF E bin edges
1	chi-square factor
1000000	Max Num of iter. in L-BFGS-B
3,1	3 = use RF bin structure, 1 = dF/dE

The expectation value $<\chi^2>$ of χ^2 should equal to the number of degrees of freedom involved, which in this case is equal to the number of energy bins in the measurement set. This is further specified to be the final chi-squared per degree of freedom, therefore this parameter was set equal to one.

The responses from the MCNP – PoliMi code are reasonable but not very accurate compared to the response functions of UMG where unfolding neutron energy spectra at the proton edge result in energies differing on average by over 70%. One reason for this could be the application of the post processing code algorithm which uses a quadratic fit to expand the light function for radiation energy deposition.

$$L_{hydrogen} = 0.0350E_n^2 + 0.1410E_n \qquad \text{Equation 7}$$

$$L_{carbon} = 0.02E_n \qquad \text{Equation 8}$$

Equations 7 – 8 show the light function fits as a function of neutron energy deposition on hydrogen (MeV) where L is the measure light output (MeVee). The neutron interactions with carbon are assumed to generate a small light output on the order of two percent of the incident energy[xvii]. This agrees with the alpha particle reaction products for high

ionization density but not as true when neutron energy rises above 8 MeV, the beginning of the regime where alpha particle light output begins to take a larger role in overall scintillation light output[xviii]. Additionally, this could be due to the uniqueness of the detector response functions. As stated earlier it was outside the scope of this project to experimentally obtain the response functions for the specific NE-213 detector used in this work.

Tabulated and Graphical Unfolding Results

The calibration run with ^{22}Na source pulse height spectrum was background corrected and analyzed, shown in Fig. 17. Depicted in Fig. 18, the half-height of the corresponding energy due to the Compton edge was assigned to the 0.511 and 1.275 MeV of each peak. A straight line fit was applied to the extrapolated data to form the calibrated energy spectra for the associated gain run of the detector which assigned a pulse height energy to each channel number in the measured data and this is shown in Fig. 19. A ^{60}Co source measurement was used to assess the uncertainty in the location of its Compton edge. A change of less than 0.001 σ was found for the fit when including the calibration data from the ^{60}Co run.

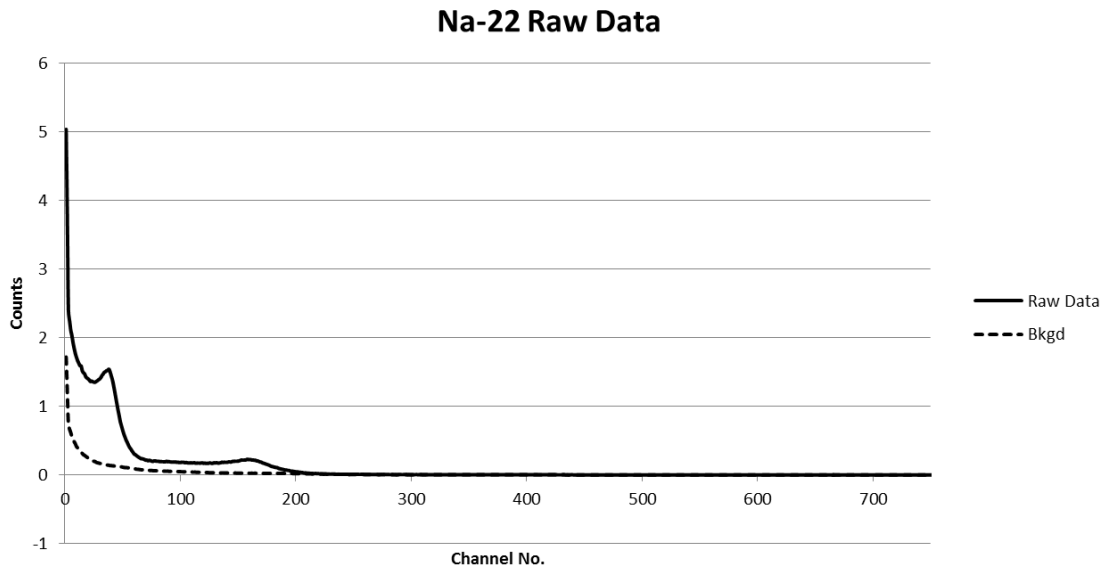

Figure 17. The Na-22 spectrum is shown along with the background measurement.

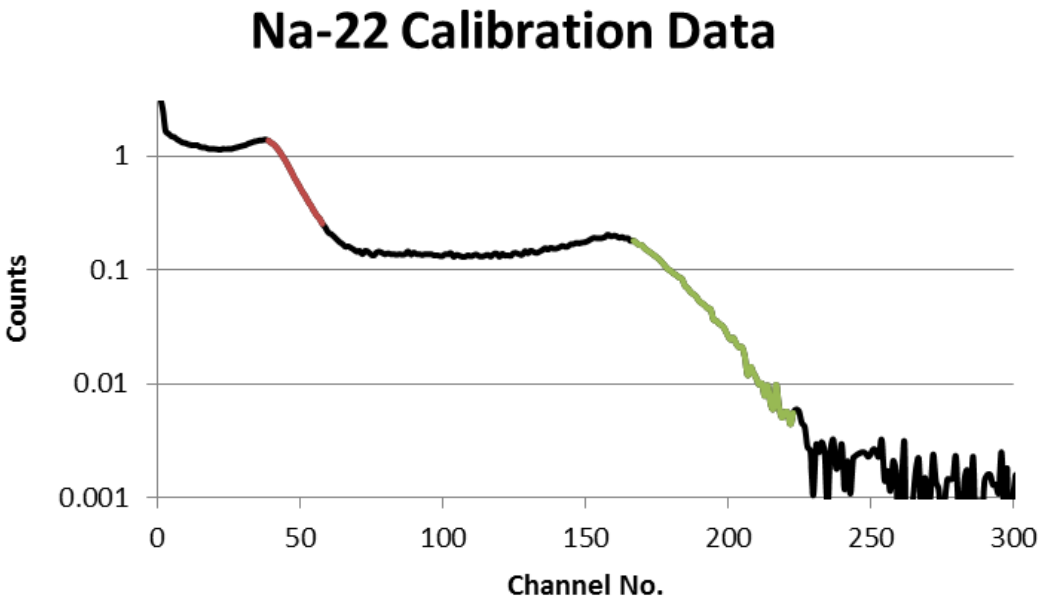

Figure 18. The Na-22 spectrum peaks are highlighted since the acquired spectrum must be analyzed for calibration. Taking the half height of each peak yields the channel number corresponding to the peak energy.

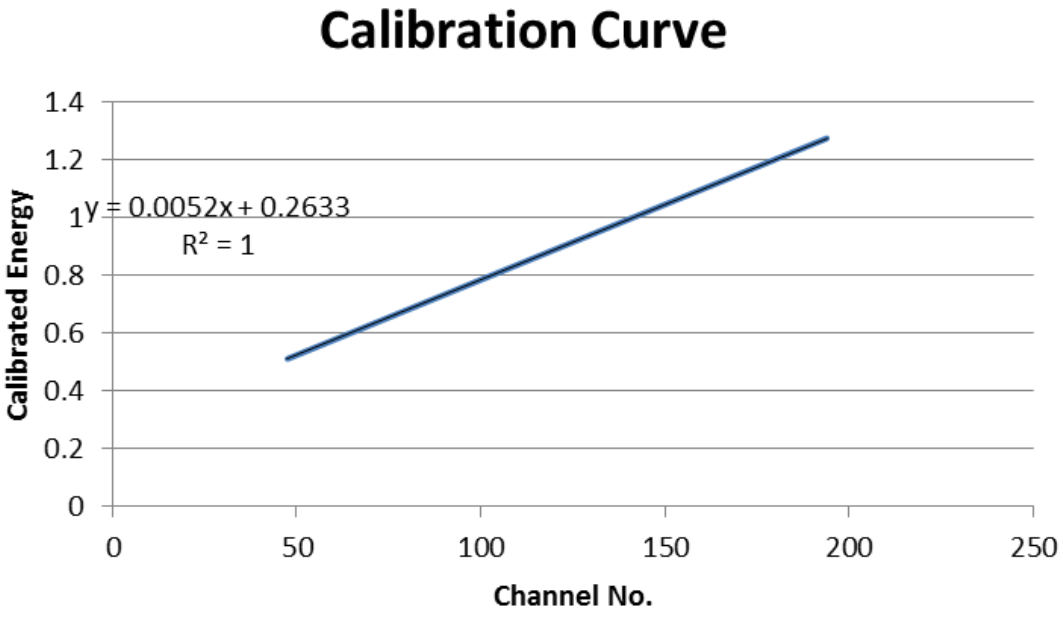

Figure 19. The Na-22 spectrum calibration is shown.

Gamma Rejection Ratio

By separating the gated neutron measurement counts for the AmBe source and the gated neutron measurement counts for the ^{22}Na source and comparing the results the gamma rejection ratio was found to be 1.6%. Thus the counts bledding into the neutron window due to incident gamma radiation average to 1.6% of the total number of counts when using the timing characteristics to allow only gated neutron pulses. This ratio drops off drastically as the intensity of the tail end of the light pulse is increased and discrimination becomes more defined. At energies greater than 500 keV the false positive counts due to gamma radiation become negligible. This was derived be recording the number of counts with the neutron gate open and closed for a measurement of the gamma source.

Uncertainty Modeling

After the calibration is completed, the measurement data were normalized and background corrected. The error associated with each measurement bin was assumed to increase as the energy increased so the epistemic error was modeled to trend toward exponentially increasing as the measured energy magnitude of the channel increased. However, the counting uncertainty was also taken into account. As the number of counts decreases the uncertainty associated with the value increase. This can be modeled to trend as a power law decreasing uncertainty as counts increase. This approach is more complex than taking the square root of the measurement value to predict the standard deviation. Thus the uncertainty involved with each successive measurement value was evaluated with the following equation.

$$Error_i = 0.0082 x_i^{0.527} + A \qquad \text{Equation 9}$$

Using the above approximation, x_i is the counts for energy bin number i and A is a constant value for the minimized uncertainty set at 6.41315E-05.

Unfolded Spectra

A measurement of two reference neutron fields was performed with the detection system, unmoderated Cf-252 and heavy-water moderated Cf-252. Once the unfolded solutions matched the expected output, the AmBe source was measured and unfolded. The experimental results for the raw AmBe measurement data can be seen in Fig. 20. To discriminate between the neutron and gamma signals, the Time-to-Amplitude converter output was analyzed and is depicted in Fig. 21. This shows a small amount of overlap between the larger gamma peak and the smaller neutron peak yielding inherent error from the overlap. This error was taken into account in the gamma rejection ratio analysis. After acquiring the measurement data for the AmBe spectrum at low gain settings a similar measurement was run at high gain settings. This change allowed for the low energy peaks of the AmBe spectrum to be unfolded. The high and low gain measurement data can be seen in Fig. 22 and 23.

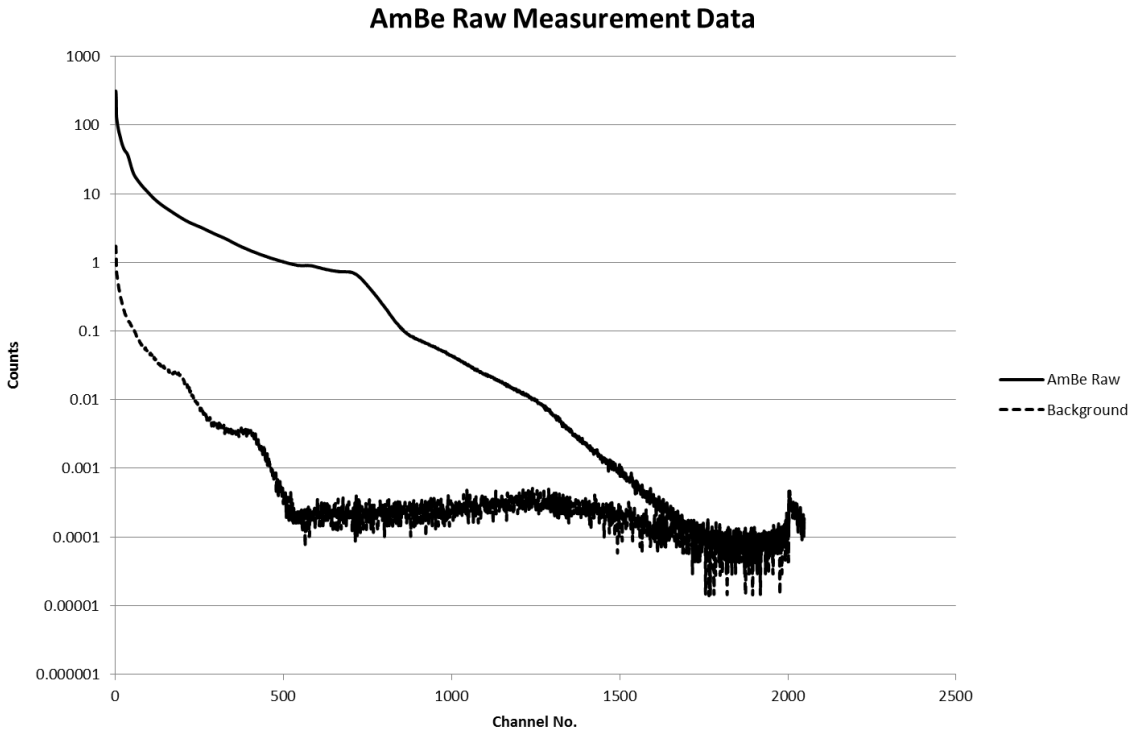

Figure 20. Raw measurement data recorded from the organic scintillator irradiated with the AmBe source.

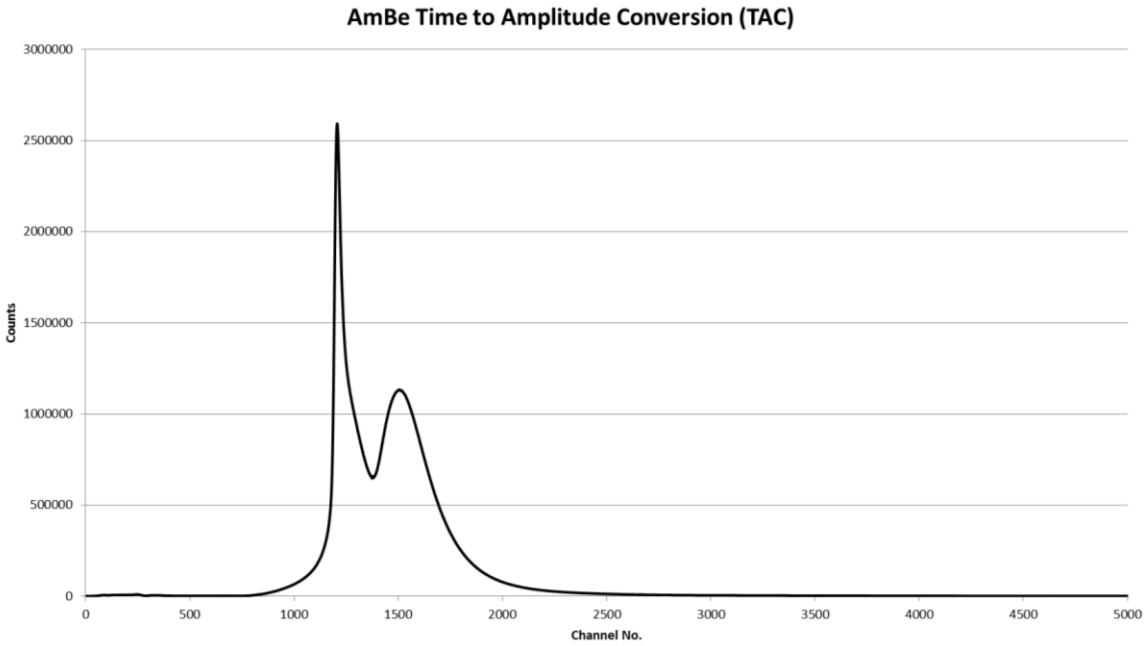

Figure 21. The Time-to-Amplitude output shows the discrimination capability between neutrons and gammas from the organic scintillator irradiated with the AmBe source.

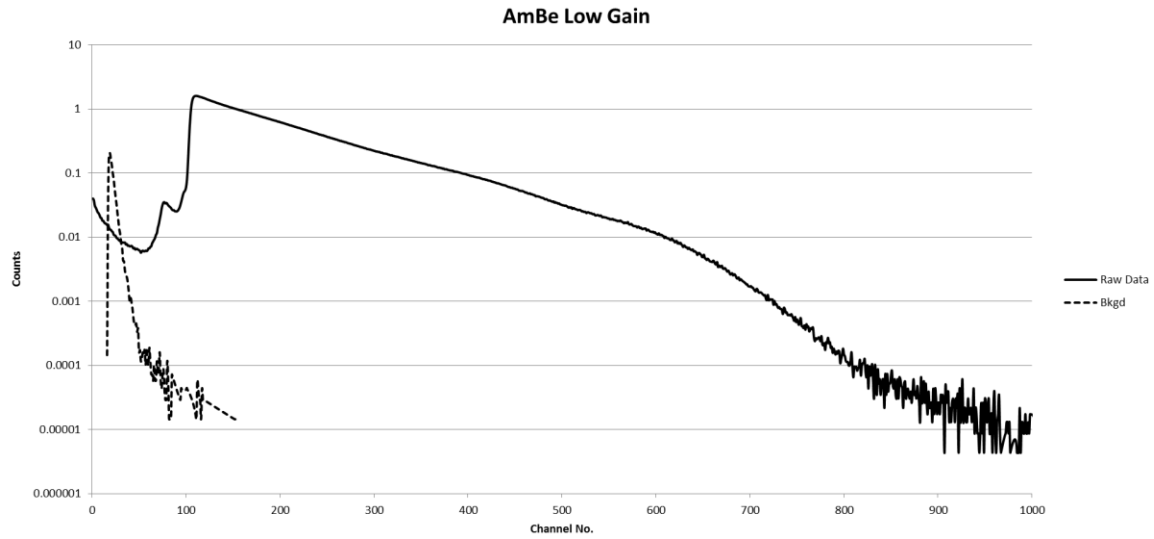

Figure 22. Raw measurement data recorded with neutron gating and low gain settings from the organic scintillator irradiated with the AmBe source.

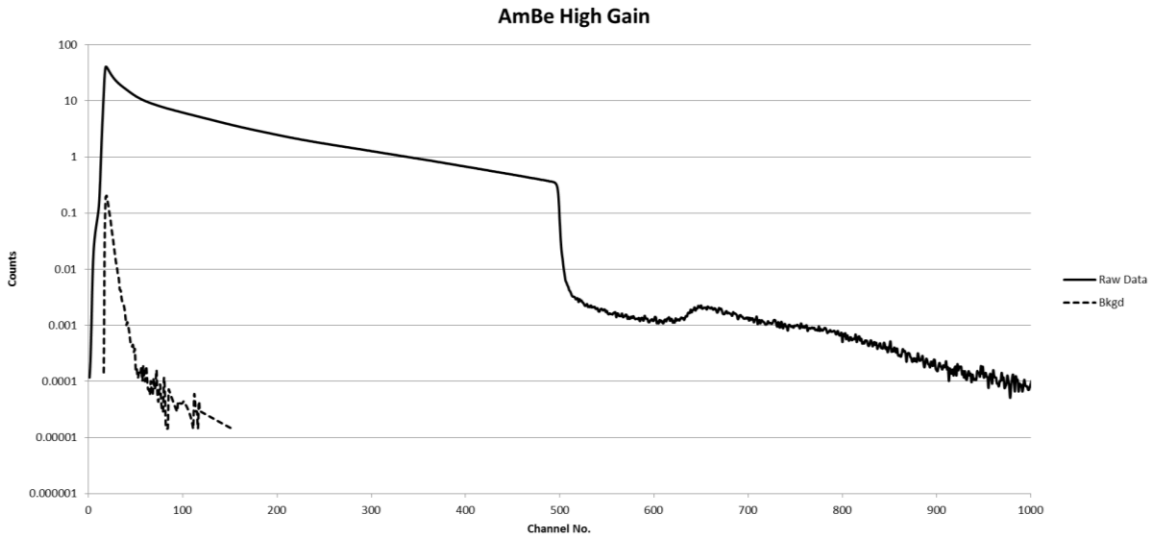

Figure 23. Raw measurement data recorded with neutron gating and high gain settings from the organic scintillator irradiated with the AmBe source.

The AmBe neutron spectral response was unfolded using the MAXED_MC33 computer code and was found to be in good agreement with published AmBe spectra data[xix]. The measured data were obtained from high and low gain measurements to include all low energy and high energy counts detectable. The low gain measurement results were unfolded to obtain neutron energy spectra above 2 MeV. This approach resolved four distinct peaks above this energy, however the unfolded results were terminated for energies below this energy. Thus high gain measurements were included. The high gain measurement results were unfolded to improve the accuracy of the results below 2 MeV. This approach resolved two distinct peaks below this energy.

Additionally, to confirm the shape of the unfolded spectra a flat starting spectra was used. As for the two reference neutron fields, the pulse heights recorded were generated by incident neutrons by only allowing pulses with the timing characteristics of proton recoil to be tallied. Figure 24 – 35 shows the unfolded AmBe spectrum together with the incident neutron spectrum, a default spectrum, and the measured spectrum. These graphs were unfolded using the UMG response functions for error reduction. Figure 24 shows a combination of the high and low gain unfolded results. A comparison of the combined unfolded results with previously published data on unfolded PuBe and AmBe neutron spectrum is shown in Figures 27, 29, and 35. The results from this study are seen to accurately reproduce the AmBe spectrum. The PuBe neutron spectrum is included since the beryllium neutron energy spectrum will not differ by much when changing the alpha source.

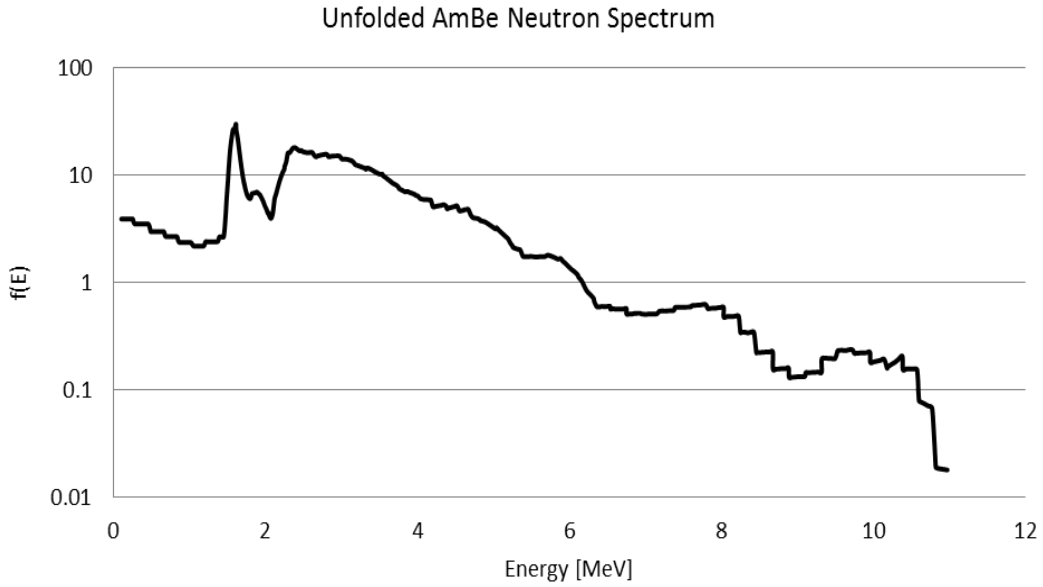

Figure 24. A combination of the unfolded spectral responses for the high and low gain settings on logarithmic scale showing the resolved peaks below 2 and above 8 MeV.

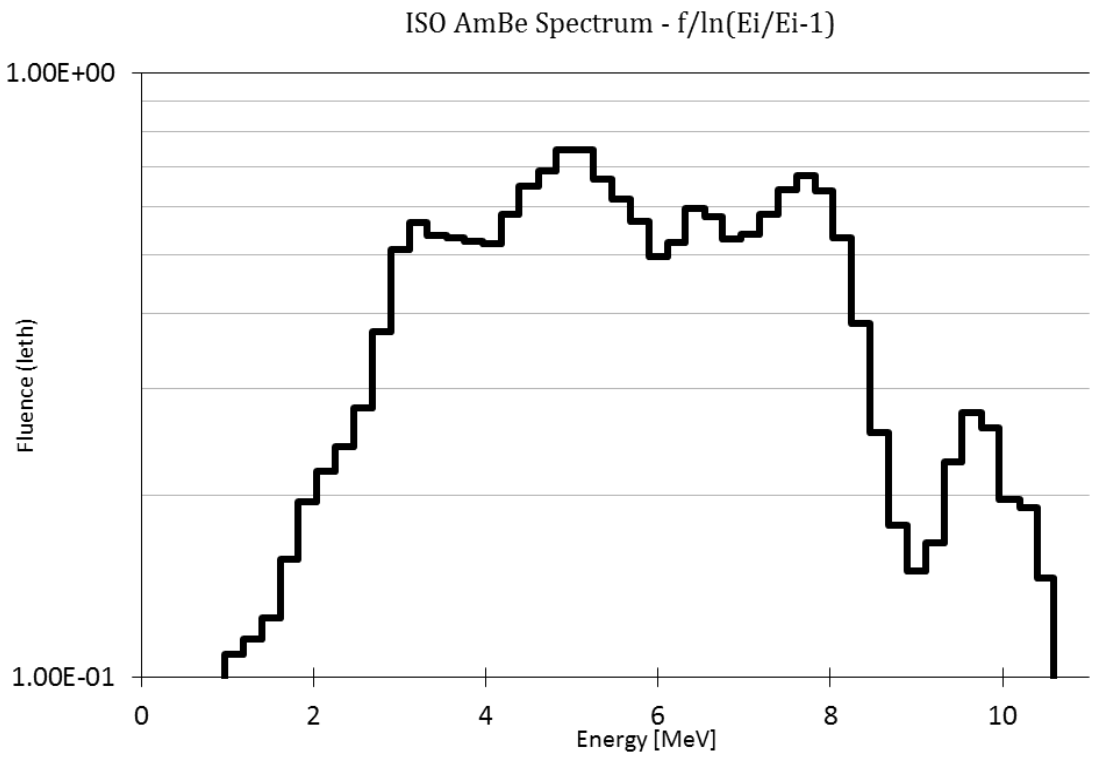

Figure 25. The ISO 8529 Standard of the AmBe neutron spectrum.

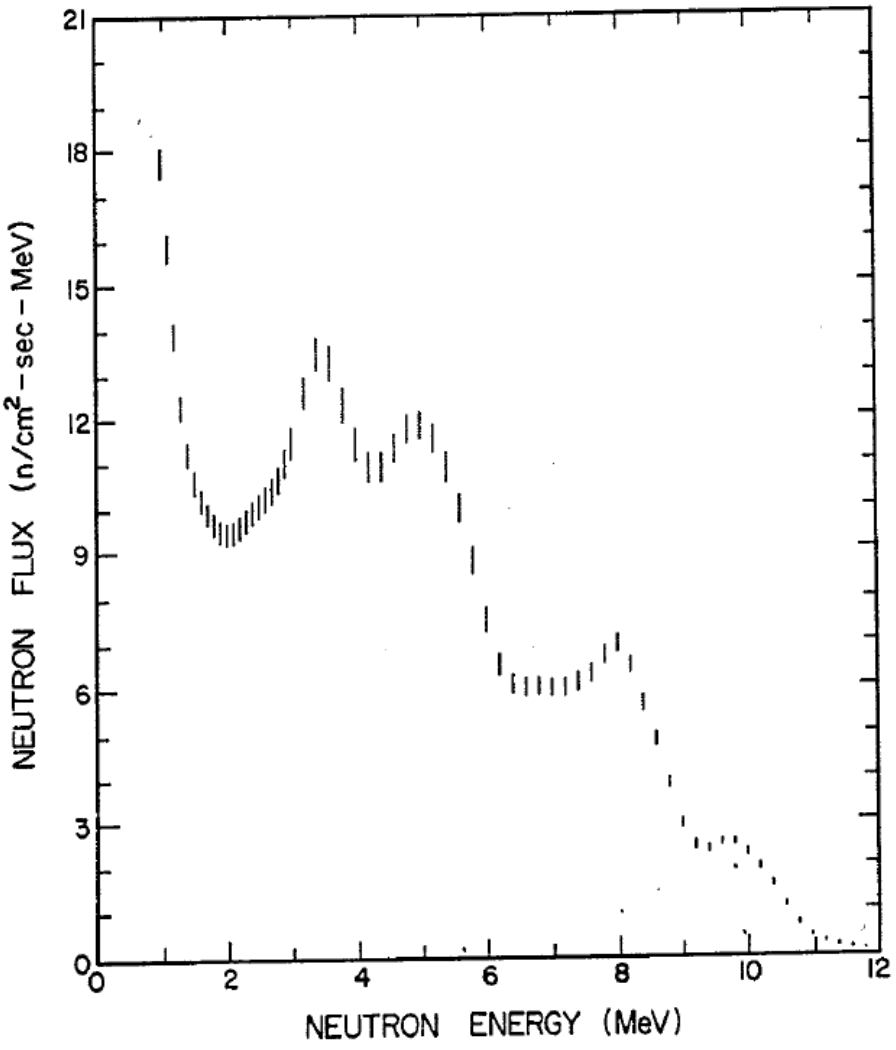

Figure 26. A comparison of the unfolded spectral response and the first iteration neutron spectrum of a 5-Curie PuBe source using FORIST.[xx]

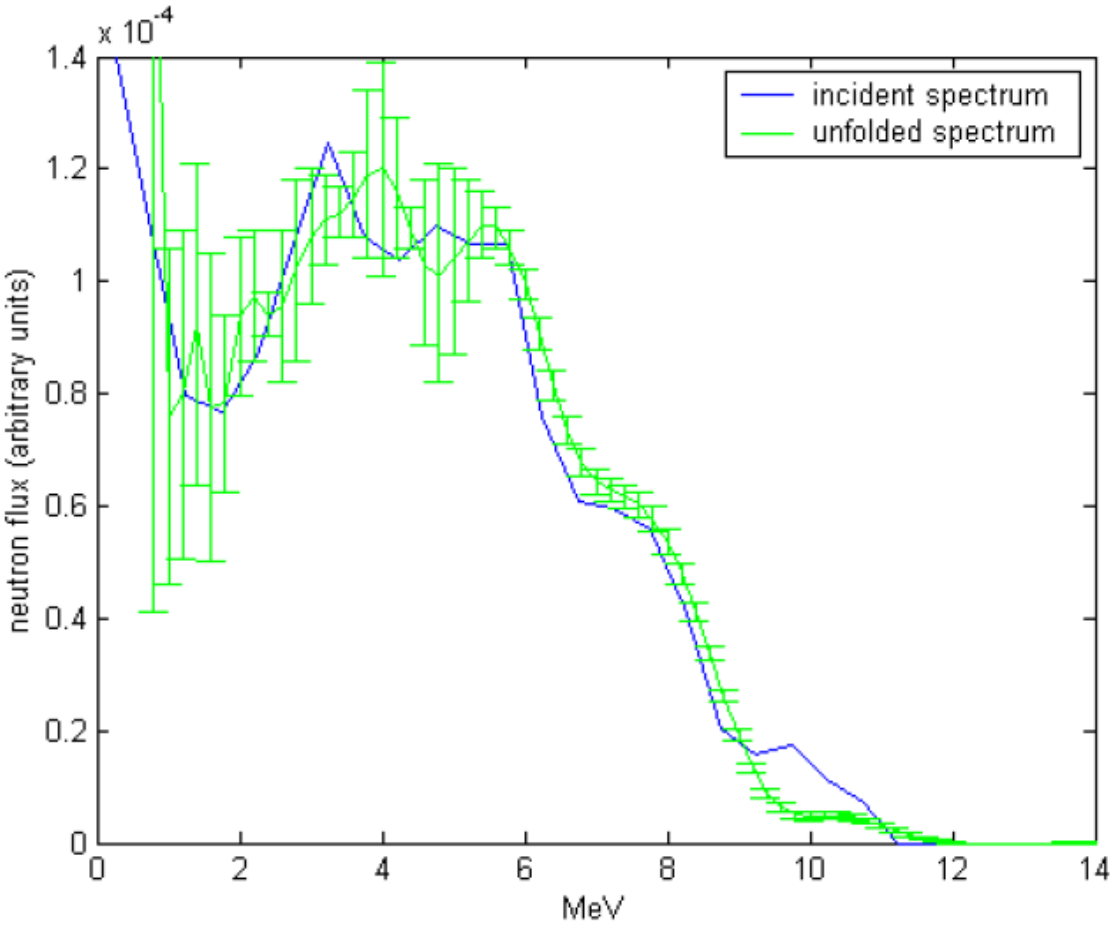

Figure 27. A comparison of the unfolded spectral response and the first iteration neutron spectrum of an AmBe source using MCNP-PoliMi.[xxi]

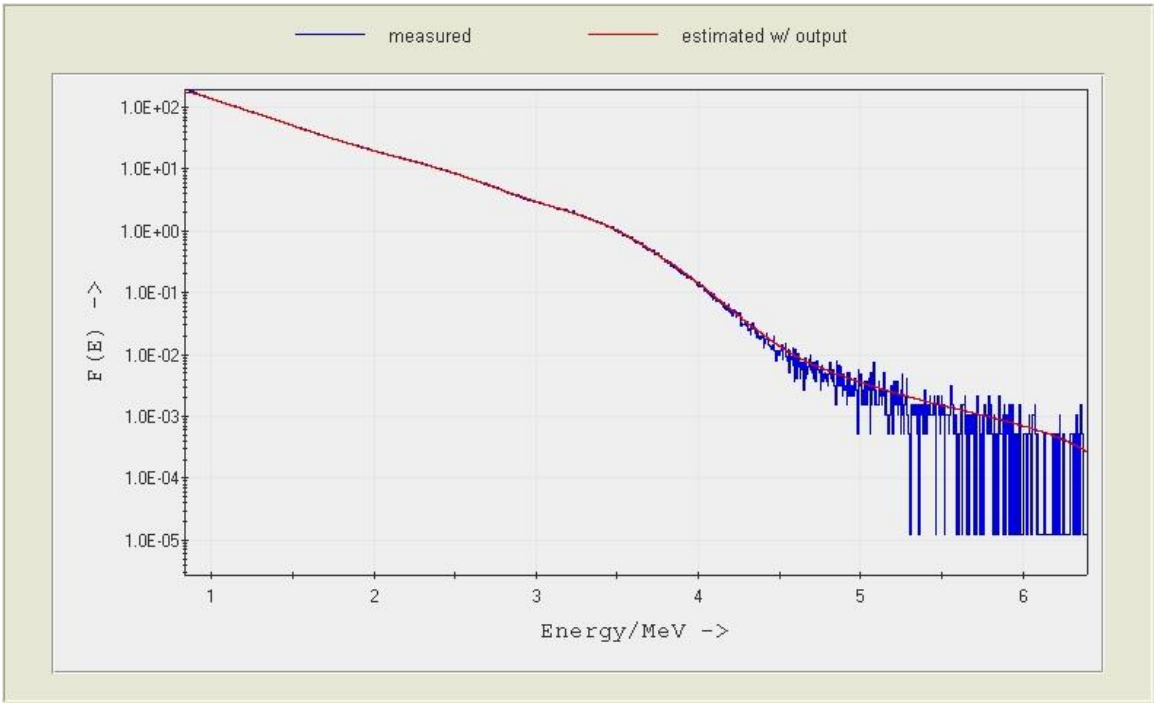

Figure 28. A comparison of the measured spectral response and the best approximation spectrum on logarithmic scale estimated with the response functions for the low gain measurement of the AmBe source.

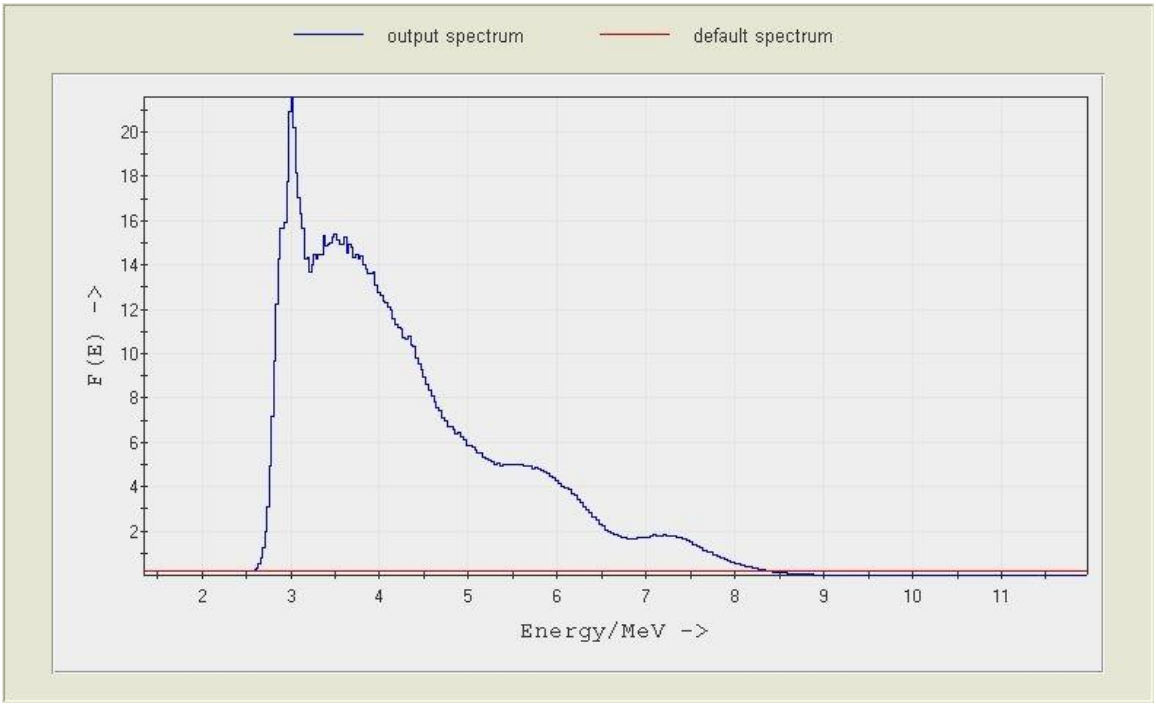

Figure 29. A comparison of the unfolded spectral response and the default spectrum for the low gain measurement of the AmBe source.

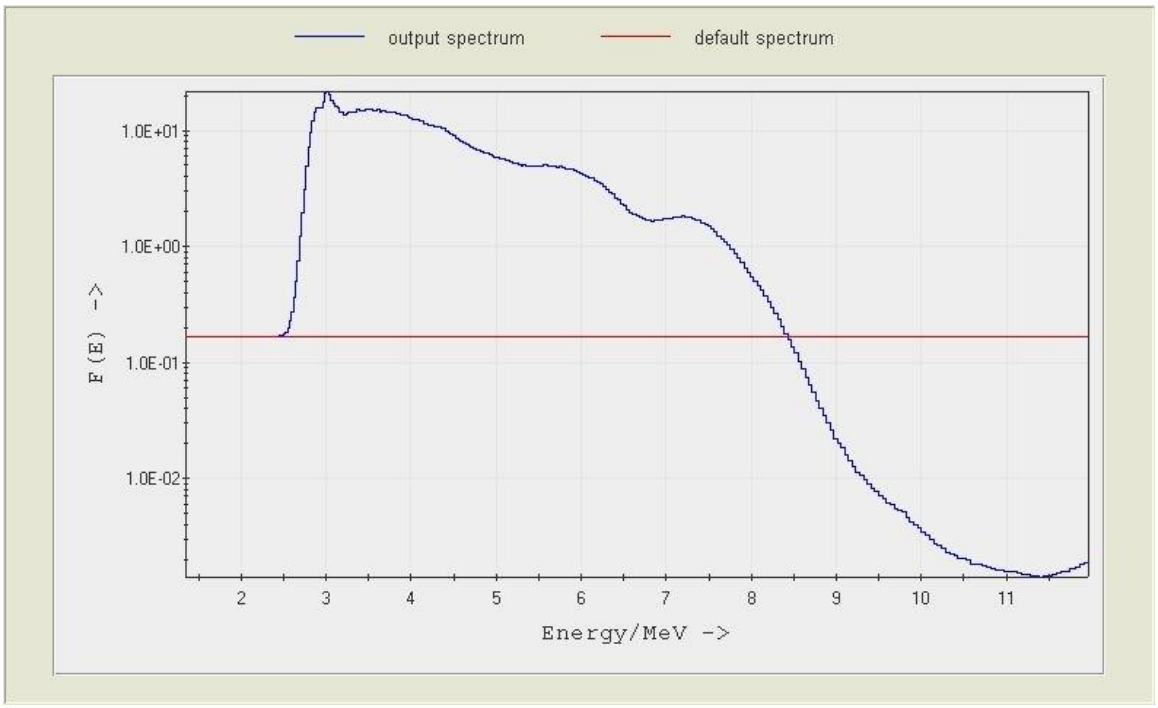

Figure 30. A comparison of the unfolded spectral response and the default spectrum on logarithmic scale for the low gain measurement of the AmBe source.

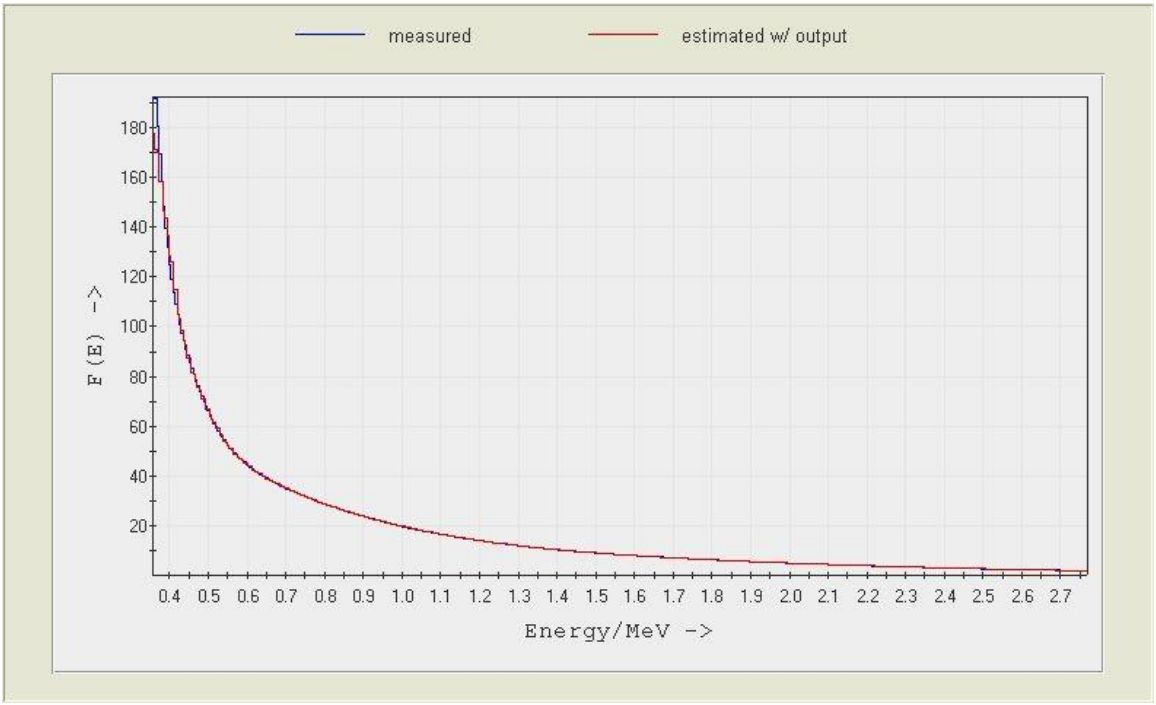

Figure 31. A comparison of the measured spectral response and the best approximation spectrum estimated with the response functions for the high gain measurement of the AmBe source.

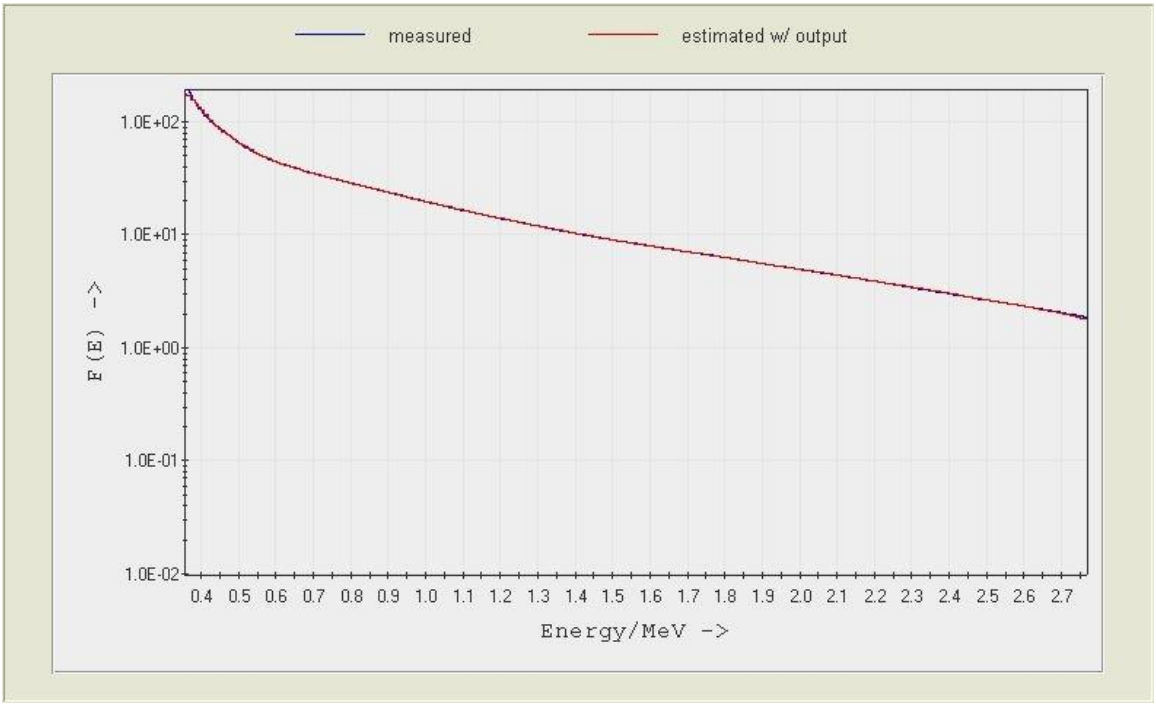

Figure 32. A comparison of the measured spectral response and the best approximation spectrum estimated with the response functions on logarithmic scale for the high gain measurement of the AmBe source.

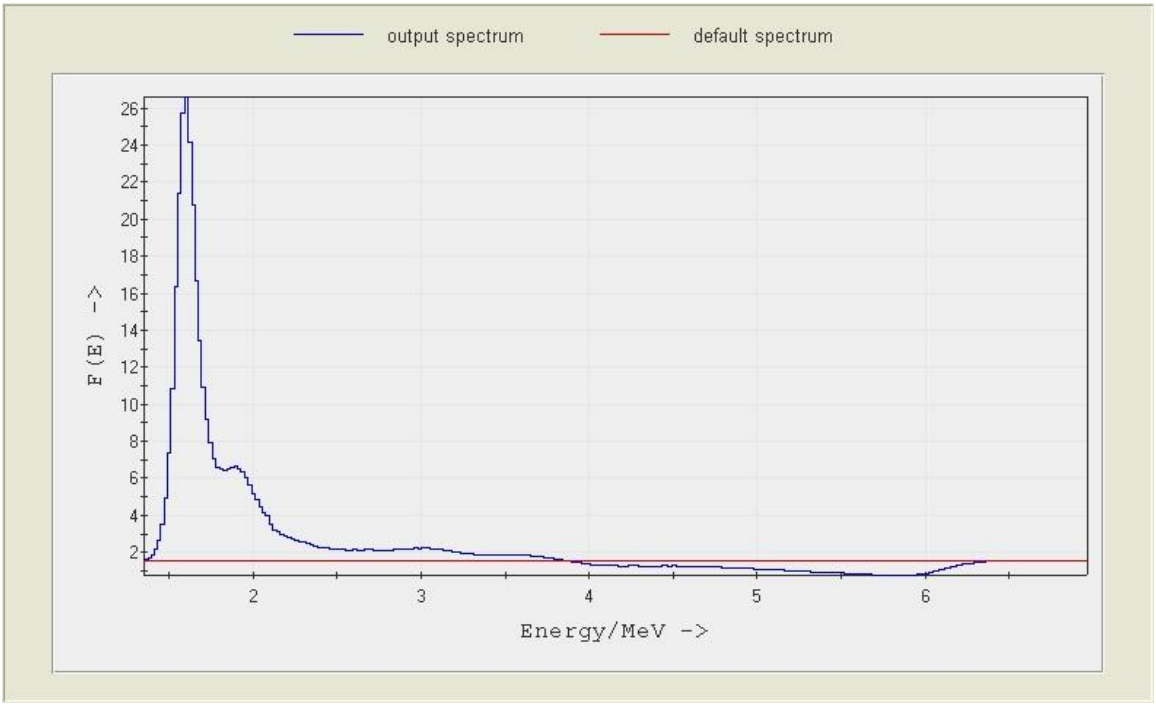

Figure 33. A comparison of the unfolded spectral response and the default spectrum for the high gain measurement of the AmBe source.

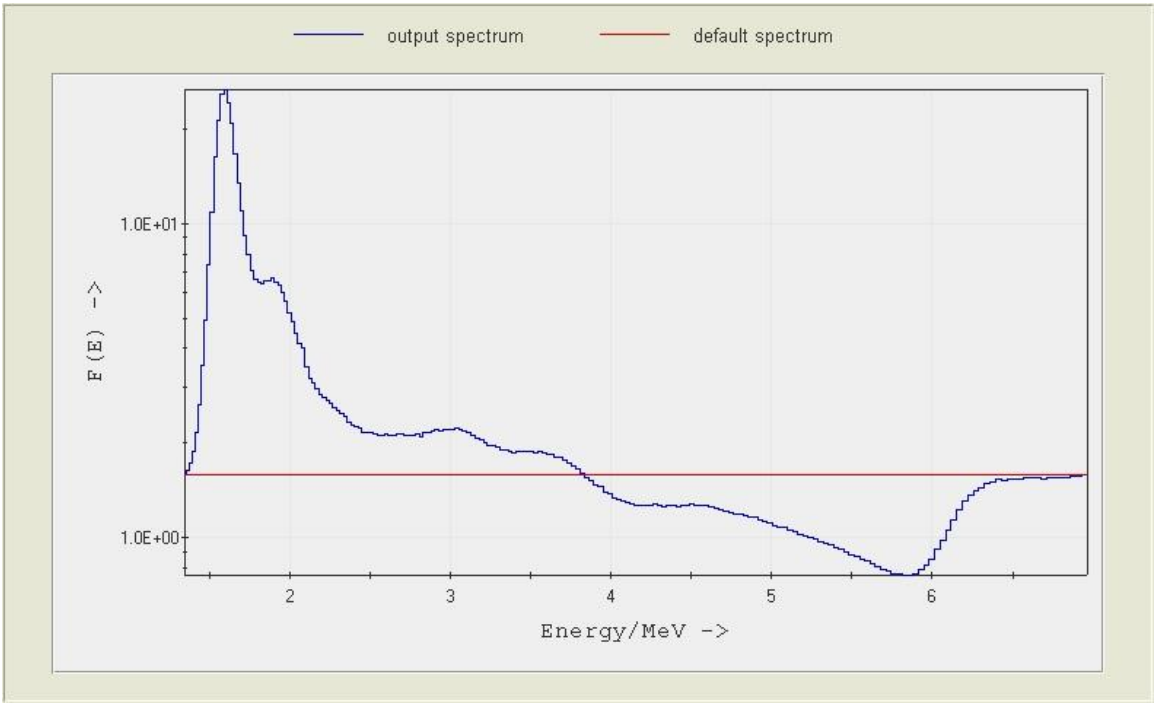

Figure 34. A comparison of the unfolded spectral response and the default spectrum on logarithmic scale for the high gain measurement of the AmBe source.

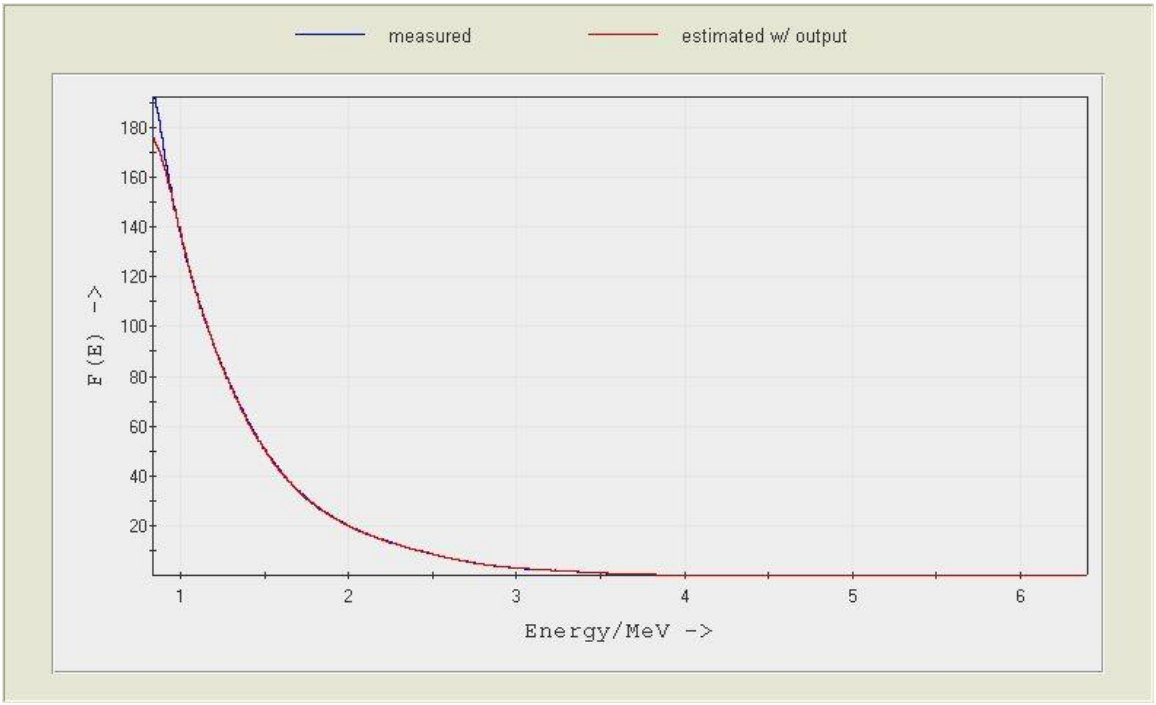

Figure 35. A comparison of the measured spectral response and the best approximation spectrum estimated with the response functions for the low gain measurement of the AmBe source.

These graphs were unfolded using the UMG package code MAXED_MC33. To confirm the shape of the unfolded spectra the results were compared with more recent unfolded data[xxi]. Fig. 24 shows essentially identical results for the neutron spectra as published results. Additionally, Fig. 33-34 extrapolate on an unanalyzed energy region below 2 MeV and shows two distinct energy peaks at low energies. The data matches with well with a separate publication for americium beryllium unfolding results[xvi].

CHAPTER 5

CONCLUSIONS

In this work, an organic scintillator detection system were assembled which accurately performs neutron-gamma separation. The system allows storage of the neutron-induced and gamma-induced recoil spectra separately. An unfolding code was implemented to deconvolute neutron induced pulse-height spectra into a neutron flux spectrum. In order to verify the performance of the system, measurements of two reference neutron fields were performed with the system, unmoderated Cf-252 and heavy-water moderated Cf-252. After the operation of the detection system was verified, measurements were made of an AmBe neutron source. The goal of this thesis work was to investigate system design and create a functioning NE-213 detection system at Georgia Tech. Careful analysis on the response functions used to unfold measured data were accomplished with a comparison of the existing response functions and a new set of response functions derived from the MCNP – PoliMi code. By creating an integrated detection system and by formatting this thesis as a NE-213 detection system procedure, a reduction in work necessary to successfully unfold measured neutron data has been accomplished. The work focused on creating NE-213 detector system that can be used in a mixed radiation field environment and the associated tasks and steps required to fully deconvolute the data. The results are encouraging and will be used in a variety of neutron spectroscopy measurements.

CHAPTER 6

FUTURE WORK

The gathering and unfolding of recorded neutron data can be made more efficient with the addition of recently purchased equipment. As part of the continuing work under this project, the mesytec MPD-4 four channel pulse shape discriminator module for NIM bin will be combined with a MADC-32 Multichannel Peak Sensing ADC controlled by a VM-USB VME controller with USB interface mounted in VME crate. The new equipment will increase data throughput as well as increasing conversion, reducing dead time and improving data collection.

APPENDIX A

DESCRIPTION OF DEFAULT SUBHEADING SCHEME

Table 1. Range of Protons in Organic Scintillator[xxii]

Ion Energy	Projected Range
500.00 keV	7.58 um
1.00 MeV	22.08 um
2.00 MeV	67.93 um
3.00 MeV	35.13 um
4.00 MeV	22.39 um
5.00 MeV	28.68 um
6.00 MeV	53.38 um
7.00 MeV	95.95 um
8.00 MeV	55.78 um
9.00 MeV	32.68 um
10.00 MeV	1.13 mm

Example Input File for MCNP – PoliMi

One liquid scintillator, monoenergetic neutron source

c cell cards

1 1 -0.874 20 -21 -30 31 -40 41 imp:n,p,e=1 $ detector

2 0 (#1) -100 101 -102 103

-104 105 imp:n,p,e=1 $ void

3 0 100:-101:102:-103:

104:-105 imp:n,p,e=0 $ everything else

c 2.00"=5.08 cm

c detector left of source 100 cm

20 px -105.08 $ left side of detector

21 px -100 $ right side of detector towards source

```
c detector depth
30  py   2.54            $ front of detector
31  py  -2.54            $ rear of detector
c
c detector heights
40  pz   2.54            $ top of detector
41  pz  -2.54            $ bottom of detector
c
c rest of universe
100  pz   5.00           $ top of box
101  pz  -5.00           $ bottom of box
102  py   5.00           $ rear of box
103  py  -5.00           $ front of box
104  px   5.00           $ right side of box
105  px  -110            $ left side of box

mode n p e               $ neutron electron photon mode
c Materials
m1                  $ organic scintillator (0.874 g/cc)
    6000.60c  1       $ C
    1001.60c  1.212   $ H
SDEF POS=0 0 0
    RAD=D1
    ERG=0.04
SI1 0   1
SP1 -21 2
c ! The following two PHYS cards and CUT:P are essential for analog MC
```

```
PHYS:N J 20.
PHYS:P 0 1 1
c The following CUT cards kill neutrons and photons having times
c exceeding 2000 ns after the originating source event
CUT:N 200
CUT:P 2J 0
FC8 Pulse Height Distribution by Neutrons in Detector
F8:N 1
E8 0 1e-6 1e-3 0.01 1000I 10
FC6 Energy Deposition by Neutrons in Detector
F6:N 1
E6 0 1e-6 1e-3 0.01 1000I 10
FC4 Spectral Fluence by Neutrons in Detector
*F4:N 1
E4 0 1e-6 1e-3 0.01 1199I 12
FC11 Neutron Current entering the front face of the detector
F11:N 21
C11 0 1
FC21 Photon Current entering the front face of the detector
F21:P 21
C21 0 1
CTME 10
IPOL 0 0 1 0 2J 1 1
RPOL 1e-4 1e-4 J 1     $ Recoil energy set to ON by putting forth parameter equal to 1
FILES 21 DUMN1
```

Example Output File with Collision Information for MCNP-PoliMi

2227	1	1	-99	1001	1	3.828774	2.12	-100.06	0.99	-1.67	1.000E+00	0	0	0 1.200E+01
5157	1	1	-99	1001	1	4.849263	2.12	-100.23	1.68	1.57	1.000E+00	0	0	0 1.200E+01
21948	1	1	-99	6000	1	0.132884	2.17	-103.10	0.03	2.47	1.000E+00	0	0	0 1.200E+01
34255	1	1	-1	6000	1	1.268222	2.20	-104.67	-1.74	1.86	1.000E+00	0	0	0 1.200E+01
34255	1	1	-99	1001	1	0.912901	2.29	-104.31	-2.47	0.81	1.000E+00	0	0	10 1.096E+00
34255	1	1	-99	1001	1	0.174329	2.70	-104.88	-1.49	-1.32	1.000E+00	0	1	10 1.829E-01
34255	1	1	-99	1001	1	0.000368	3.08	-104.44	-1.41	-1.52	1.000E+00	0	2	10 8.658E-03
34255	1	1	-99	1001	1	0.003953	3.47	-104.03	-1.40	-1.79	1.000E+00	0	3	10 8.270E-03
34255	1	1	-99	1001	1	0.003681	4.28	-103.79	-1.03	-2.38	1.000E+00	0	4	10 4.305E-03
34255	1	1	-99	1001	1	0.000191	4.47	-103.78	-1.06	-2.43	1.000E+00	0	5	10 6.274E-04
34255	1	1	-99	1001	1	0.000425	4.81	-103.72	-1.12	-2.48	1.000E+00	0	6	10 4.435E-04
77356	1	1	-99	6000	1	0.179876	2.17	-103.24	0.92	0.51	1.000E+00	0	0	0 1.200E+01
144443	1	1	-1	6000	1	2.547141	2.15	-102.67	1.78	0.09	1.000E+00	0	0	0 1.200E+01
149337	1	1	-99	1001	1	8.960438	2.16	-103.08	-2.39	2.15	1.000E+00	0	0	0 1.200E+01
149337	1	1	-99	1001	1	2.490383	2.24	-104.06	-1.12	1.28	1.000E+00	0	1	0 3.039E+00
149337	1	1	-99	1001	1	0.426773	2.42	-103.23	-0.37	-0.21	1.000E+00	0	2	0 5.489E-01
149337	1	1	-99	1001	1	0.000405	2.44	-103.12	-0.35	-0.20	1.000E+00	0	3	0 1.221E-01
149337	1	1	-99	6000	1	0.003573	2.54	-102.63	-0.27	-0.21	1.000E+00	0	4	0 1.217E-01
149337	1	1	-99	1001	1	0.066657	2.57	-102.55	-0.21	-0.26	1.000E+00	0	5	0 1.182E-01
149337	1	1	-99	6000	1	0.005401	2.97	-101.59	-0.55	-0.99	1.000E+00	0	6	0 5.148E-02
149337	1	1	-99	1001	1	0.029712	3.16	-101.74	-0.97	-1.33	1.000E+00	0	7	0 4.608E-02
149337	1	1	-99	6000	1	0.004578	3.16	-101.74	-0.97	-1.34	1.000E+00	0	8	0 1.634E-02
149337	1	1	-99	1001	1	0.006446	3.31	-101.74	-1.04	-1.13	1.000E+00	0	9	0 1.174E-02
149337	1	1	-99	1001	1	0.004832	6.31	-103.43	-0.31	1.27	1.000E+00	0	10	0 5.317E-03
149337	1	1	-99	1001	1	0.000374	9.85	-104.37	0.01	0.87	1.000E+00	0	12	0 4.669E-04
152027	1	1	-99	6000	1	3.047587	2.17	-103.75	0.03	-0.48	1.000E+00	0	0	0 1.200E+01
152027	1	1	-1	6000	1	0.203730	2.24	-101.65	-1.89	-0.53	1.000E+00	0	1	0 8.952E+00
159915	1	1	-99	6000	1	0.024198	2.19	-103.59	-0.78	2.51	1.000E+00	0	0	0 1.200E+01
184996	1	1	-99	6000	1	0.370198	2.14	-101.15	-0.68	1.07	1.000E+00	0	0	0 1.200E+01
184996	1	1	-99	1001	1	4.554560	2.17	-102.25	-0.54	1.86	1.000E+00	0	1	0 1.163E+01
184996	1	1	-1	6000	1	1.110957	2.18	-102.54	-0.54	1.85	1.000E+00	0	2	0 7.075E+00
209640	1	1	-99	1001	1	7.800397	2.12	-100.55	2.23	-2.47	1.000E+00	0	0	0 1.200E+01
259916	1	1	-99	1001	1	6.034227	2.15	-100.96	1.64	1.79	1.000E+00	0	0	0 1.200E+01
263322	1	1	-99	6000	1	0.139837	2.14	-101.27	1.95	-0.39	1.000E+00	0	0	0 1.200E+01

280841 1 1 -99 6000 1 0.022596 2.15 -102.47 -2.23 1.35 1.000E+00 0 0 0 1.200E+01

280841 1 1 -99 1001 1 11.231592 2.17 -103.67 -2.44 1.40 1.000E+00 0 1 0 1.198E+01

280841 1 1 -99 1001 1 0.644115 2.24 -103.89 -2.12 2.07 1.000E+00 0 2 0 7.455E-01

294232 1 1 -1 6000 1 0.098331 2.13 -101.25 -0.37 -2.18 1.000E+00 0 0 0 1.200E+01

306614 1 1 -99 1001 1 4.489806 2.22 -104.85 -1.36 1.19 1.000E+00 0 0 0 1.200E+01

329258 1 1 0 2004 1 4.360347 2.12 -100.22 1.84 -0.44 1.000E+00 0 0 0 1.200E+01

329258 1 1 0 4000 1 1.937653 2.12 -100.22 1.84 -0.44 1.000E+00 0 0 0 1.200E+01

336719 1 1 -99 1001 1 5.049375 2.17 -103.18 1.14 1.28 1.000E+00 0 0 0 1.200E+01

340571 1 1 -99 1001 1 6.191754 2.17 -102.95 0.63 0.44 1.000E+00 0 0 0 1.200E+01

340571 1 1 -99 1001 1 0.885675 2.21 -103.84 -0.28 0.33 1.000E+00 0 1 0 5.808E+00

353475 1 1 -99 1001 1 10.222888 2.20 -104.30 -0.98 -2.13 1.000E+00 0 0 0 1.200E+01

360243 1 1 -1 6000 1 1.767769 2.12 -101.06 -1.08 -1.08 1.000E+00 0 0 0 1.200E+01

371248 1 1 -99 1001 1 10.402931 2.13 -100.92 1.67 0.64 1.000E+00 0 0 0 1.200E+01

371248 1 1 -99 1001 1 0.843577 2.14 -100.96 1.70 0.55 1.000E+00 0 1 0 1.596E+00

385497 1 1 -99 6000 1 0.200951 2.16 -102.62 1.72 0.71 1.000E+00 0 0 0 1.200E+01

396664 1 1 -99 6000 1 0.296783 2.13 -101.61 -1.56 -1.62 1.000E+00 0 0 0 1.200E+01

405496 1 1 -99 6000 1 0.057397 2.15 -101.20 1.11 1.06 1.000E+00 0 0 0 1.200E+01

450516 1 1 -1 6000 1 1.800381 2.14 -102.32 -1.69 -0.01 1.000E+00 0 0 0 1.200E+01

451253 1 1 -99 1001 1 3.267311 2.20 -104.88 1.64 2.37 1.000E+00 0 0 0 1.200E+01

472679 1 1 -99 1001 1 4.063381 2.15 -102.30 -1.14 0.67 1.000E+00 0 0 0 1.200E+01

472679 1 1 0 2004 1 1.546658 2.15 -102.39 -1.14 0.73 1.000E+00 0 1 0 7.936E+00

472679 1 1 0 4000 1 0.687305 2.15 -102.39 -1.14 0.73 1.000E+00 0 1 0 7.936E+00

483412 1 1 -99 6000 1 0.641762 2.20 -104.36 0.14 1.50 1.000E+00 0 0 0 1.200E+01

502376 1 1 -99 1001 1 11.352879 2.17 -102.87 -1.76 0.64 1.000E+00 0 0 0 1.200E+01

503238 1 1 -99 6000 1 0.279497 2.10 -100.32 1.31 -1.10 1.000E+00 0 0 0 1.200E+01

…

…

…

117762063 1 1 -99 1001 1 2.651688 2.19 -103.06 0.64 -2.13 1.000E+00 0 0 0 1.200E+01

117769759 1 1 -99 1001 1 3.704378 2.17 -102.78 -1.51 -1.85 1.000E+00 0 0 0 1.200E+01

117770389 1 1 -99 1001 1 7.681810 2.17 -102.75 -1.65 -1.26 1.000E+00 0 0 0 1.200E+01

117778559 1 1 -1 6000 1 1.040047 2.16 -102.60 2.39 1.08 1.000E+00 0 0 0 1.200E+01

117778559 1 1 -99 1001 1 0.759160 2.26 -102.84 0.80 1.42 1.000E+00 0 0 10
1.324E+00

117778559 1 1 -99 1001 1 0.155143 2.33 -103.30 0.50 1.79 1.000E+00 0 1 10 5.650E-01

117778559 1 1 -99 1001 1 0.409576 2.35 -103.37 0.33 1.88 1.000E+00 0 2 10 4.098E-01

```
117792558    1  1    1  6000        1   1.049898          2.18  -103.97   -0.72   -0.37  1.000E+00    0     0     0 1.200E+01
117799558    1  1  -99  6000        1   0.061526          2.16  -101.96    1.41   -2.20  1.000E+00    0     0     0 1.200E+01
117803261    1  1  -99  1001        1   5.434588          2.12  -100.75   -1.76   -0.22  1.000E+00    0     0     0 1.200E+01
117815366    1  1  -99  6000        1   1.725895          2.14  -101.44   -0.37   -2.41  1.000E+00    0     0     0 1.200E+01
117823181    1  1  -99  1001        1   7.721166          2.18  -103.20    0.56   -1.73  1.000E+00    0     0     0 1.200E+01
117823553    1  1  -99  1001        1   0.418699          2.20  -104.02   -2.49    1.89  1.000E+00    0     0     0 1.200E+01
117823553    1  1   -1  6000        1   0.084586          2.21  -104.11   -2.49    1.91  1.000E+00    0     1     0 1.158E+01
```

Example Input File for MCNP – PoliMi Post Processing Code

```
a# ~~~~~~~~~~~~~~~~~~~~~~~~~~~~~~~~~~~~~~~~~~~~~~~~~~~~~~~~~~~~~~~~~~~~~~~~~~~~~~~~~~~~~~~~~~~~~
# ~~~~~~~~~~~~~~~~~~~~~~~~~~~~~~~~~~~~~~~~~~~~~~~~~~~~~~~~~~~~~~~~~~~~~~~~~~~~~~~~~~~~~~~~~~~~~~
#
#  Input file for MPPost
#
#  version: 2.1.0
# ~~~~~~~~~~~~~~~~~~~~~~~~~~~~~~~~~~~~~~~~~~~~~~~~~~~~~~~~~~~~~~~~~~~~~~~~~~~~~~~~~~~~~~~~~~~~~~
# ~~~~~~~~~~~~~~~~~~~~~~~~~~~~~~~~~~~~~~~~~~~~~~~~~~~~~~~~~~~~~~~~~~~~~~~~~~~~~~~~~~~~~~~~~~~~~~

# ~~~~~~~~~~~~~~~~~~~~~~~~~~~~~~~~~~~~~~~~~~~~~~~~~~~~~~~~~~~~~~~~~~~~~~~~~~~~~~~~~~~~~~~~~~~~~~
# GENERAL INFORMATION
# ~~~~~~~~~~~~~~~~~~~~~~~~~~~~~~~~~~~~~~~~~~~~~~~~~~~~~~~~~~~~~~~~~~~~~~~~~~~~~~~~~~~~~~~~~~~~~~
title          NTAL
username       GSM

# ~~~~~~~~~~~~~~~~~~~~~~~~~~~~~~~~~~~~~~~~~~~~~~~~~~~~~~~~~~~~~~~~~~~~~~~~~~~~~~~~~~~~~~~~~~~~~~
# I/O FILE INFORMATION
# ~~~~~~~~~~~~~~~~~~~~~~~~~~~~~~~~~~~~~~~~~~~~~~~~~~~~~~~~~~~~~~~~~~~~~~~~~~~~~~~~~~~~~~~~~~~~~~
polimi_det_in   dumn300  # MCNP-PoliMi detector filename
output_file            ntal300      # Desired output name
label_output           yes         # (yes/no) Place labels at the top of the output files
seperate_det_response   no          # (yes/no) Print individual distributions for each detector
list_of_pulses          no          # (yes/no) Print a list mode file of all collected pulses
event_inventory_on      no          # (yes/no) Print out a table summarizing all events in the file
collision_history       no          # (yes/no) Print summary of how collisions make pulses in the detector
```

```
overwrite_files        yes        # (yes/no) Allow the code to overwrite old files
comma_delimited        no         # (yes/no) Output files delimited by a comma

# ~~~~~~~~~~~~~~~~~~~~~~~~~~~~~~~~~~~~~~~~~~~~~~~~~~~~~~~~~~~~~~~~~~~~~~~~~~~~
# MEMORY
# ~~~~~~~~~~~~~~~~~~~~~~~~~~~~~~~~~~~~~~~~~~~~~~~~~~~~~~~~~~~~~~~~~~~~~~~~~~~~
division_size   1000    # MB, size of segments to divide the file
cushion         200     # number of lines added to the arrays to prevent overstepping arrays

# ~~~~~~~~~~~~~~~~~~~~~~~~~~~~~~~~~~~~~~~~~~~~~~~~~~~~~~~~~~~~~~~~~~~~~~~~~~~~
# DETECTOR INFORMATION
# ~~~~~~~~~~~~~~~~~~~~~~~~~~~~~~~~~~~~~~~~~~~~~~~~~~~~~~~~~~~~~~~~~~~~~~~~~~~~
time_dependent   no    # (yes/no) Perform analysis by time instead of by history
NPS      1    # NPS used in the MCNP run
detector_type          1             # Type of Detector - list for each cell number
                                #   0 = Non Active Volume (i.e. PMT)
                                #   1 = Liquid Organic Scintillator
                                #   2 = He3 (Cannot be run with other types)
                                #   3 = Plastic Organic Scintillator
                                #   4 = NaI
                                #   5 = CaF2
                                #   6 = LaBr3
threshold       0.001           # MeVee, Threshold for event detection - list for each cell number
upper_threshold   12              # MeVee, the max acceptable light for event detection - list for each cell number
detector_cell_numbers   1       # Cell numbers of the detectors
                                #   NOTE: To group cells add ( ) around the group.
                                #   There must be a space before and after each (

# ~~~~~~~~~~~~~~~~~~~~~~~~~~~~~~~~~~~~~~~~~~~~~~~~~~~~~~~~~~~~~~~~~~~~~~~~~~~~
# DETECTOR INFORMATION - Pulse Height
# ~~~~~~~~~~~~~~~~~~~~~~~~~~~~~~~~~~~~~~~~~~~~~~~~~~~~~~~~~~~~~~~~~~~~~~~~~~~~
pulse_height_on     yes      # (yes/no) Print pulse height distributions
sum_then_light      no       # (yes/no) Convert the sum of all contributing particles energy to light
cross_talk_sub_on   no   # (yes/no) Eliminate particles with cross talk

# Pulse Generation Time - ns, Light collection time for a pulse
```

```
organic_liq_pgt     10   # Pulse generation time for an organic liquid scintillator
organic_pl_pgt      10   # Pulse generation time for an organic plastic scintillator
nai_pgt             10       # Pulse generation time for a NaI detector
caf2_pgt            10   # Pulse generation time for a CaF2 detector
labr3_pgt           10   # Pulse generation time for a LaBr3 detector

# Deadtime - ns, dead time of the detector between pulses
organic_liq_dt      0   # Dead time for an organic liquid scintillator
organic_pl_dt       0   # Dead time for an organic plastic detector
nai_dt              0      # Dead time for a NaI detector
caf2_dt             0   # Dead time for a CaF2 detector
labr3_dt            0   # Dead time for a LaBr3 detector

histogram_start     0     # MeVee, Min value for the pulse height distribution
histogram_stop      12     # MeVee, Max value for the pulse height distribution
bin_step            0.001     # MeVee, Bin step - top side of the bin



# ~~~~~~~~~~~~~~~~~~~~~~~~~~~~~~~~~~~~~~~~~~~~
# ORGANIC SCINTILLATOR
# ~~~~~~~~~~~~~~~~~~~~~~~~~~~~~~~~~~~~~~~~~~~~
calibration_regions  1                          # Number of independently fit neutron light regions
region_type          1                          # Specify which form for the coefficients, if multiple regions list selections
                                        # Type    Form       How to enter values on the neutron_calibraion line
                                        #   1 = Ax^2+Bx+C  -> E1 E2 A B C
                                        #   2 = Ax^2/(x+B) -> E1 E2 B A
                                        #   3 = A(Bx-C(1-exp(Dx^E)))  -> E1 E2 A B C D E
                                        #   Where E1 and E2 are the lower and upper energy bounds respectively in MeVee
neutron_calibration  0 50     0.03495 0.1424  -0.036    # Neutron Calibration - see above for entry instructions
#               0.8 1   0 0 0.03495 0.1424  -0.036 &  #   For multiple regions add an '&' to the end of the line and continue next region
#               1   50  0 0 0.03495 0.1424  -0.036    #   on the next line
photon_calibration      1.000  0.000                # A,B: Parameters for photon light conversion - Ax+B
carbon_light_constant   0.02                        # Constant value for carbon light conversion
deuterium_calibration   0 0 0.0131 0.2009 -0.0331       # A,B,C,D,E: Parameters for deuterium light conversion - Ax^4+Bx^3+Cx^2+Dx+E
```

```
# ~~~~~~~~~~~~~~~~~~~~~~~~~~~~~~~~~~~~~~~~~~~~
# Light Output Resolution
# ~~~~~~~~~~~~~~~~~~~~~~~~~~~~~~~~~~~~~~~~~~~~
light_resolution_on   no    # (yes/no) Turns on/off the a Gaussian Light Broadening
                      #    Coefficients A,B,C for Gaussian Broadening: A*LO+B*Sqrt(LO)+C
organic_liq_p_lgt   # Resolution for photons in liquid scintillator
organic_liq_n_lgt     # Resolution for neutrons in liquid scintillator

# ~~~~~~~~~~~~~~~~~~~~~~~~~~~~~~~~~~~~~~~~~~~~
# Time Resolution
# ~~~~~~~~~~~~~~~~~~~~~~~~~~~~~~~~~~~~~~~~~~~~
tme_resolution_on   no     # (yes/no) Turns on/off time broadening
organic_liq_tme  1  # FWHM for organic liquid

# ~~~~~~~~~~~~~~~~~~~~~~~~~~~~~~~~~~~~~~~~~~~~~~~~~~~~~~~~~~~~~~~~~~~~~~~~~~~~~~~~~~~~~~~~~~~~~~~~~~~~
# TIME-OF-FLIGHT, CORRELATION, and AUTOCORRELATION INFORMATION
# ~~~~~~~~~~~~~~~~~~~~~~~~~~~~~~~~~~~~~~~~~~~~~~~~~~~~~~~~~~~~~~~~~~~~~~~~~~~~~~~~~~~~~~~~~~~~~~~~~~~~
tof_on     yes     # (yes/no) Turn on/off TOF distributions (cannot have a start detector)
cross_correlation_on     no      # (yes/no) Turn on/off cross correlation function
auto_correlation_on     no      # (yes/no) Turn on/off auto correlation function
start_detector          1       # Cell number of the start detector (leave blank for TOF)
time_start             -100    # ns, time for the correlation plot to start
time_stop               100  # ns, time for the correlation plot to stop
time_increment          1       # ns, time increment between the bins - top side of the bin
cc_window_incr          1000    # ns, time window for correlation events for time dependent analysis
# ~~~~~~~~~~~~~~~~~~~~~~~~~~~~~~~~~~~~~~~~~~~~
# Pulse Height Correlation
# ~~~~~~~~~~~~~~~~~~~~~~~~~~~~~~~~~~~~~~~~~~~~
pulse_correlation_on   no       # (yes/no) Turn on/off pulse height correlation analysis
pc_min                 0        # MeVee, Minimum value for pulse height binning
pc_max                 5        # MeVee, Maximum value for pulse height binning
pc_incr                0.05     # MeVee, increment for pulse height binning
stop_pulse_only        yes      # (yes/no) Ignore start detector pulse height

# ~~~~~~~~~~~~~~~~~~~~~~~~~~~~~~~~~~~~~~~~~~~~~~~~~~~~~~~~~~~~~~~~~~~~~~~~~~~~~~~~~~~~~~~~~~~~~~~~~~~~
```

```
# CAPTURE GATED DETECTORS
# ~~~~~~~~~~~~~~~~~~~~~~~~~~~~~~~~~~~~~~~~~~~~~~~~~~~~~~~~~~~~~~~~~~~~~~~~~~~~~~~
capture_gate_on     no   # (yes/no) Capture gated detector response on/off
cap_low             0          # ns, start time for binning the time to capture histogram
cap_high            2000       # ns, stop time for binning the time to capture histogram
cap_incr            10         # ns, bin size the time to capture histogram

# ~~~~~~~~~~~~~~~~~~~~~~~~~~~~~~~~~~~~~~~~~~~~~~~~~~~~~~~~~~~~~~~~~~~~~~~~~~~~~~~
# He3 MODULE
# ~~~~~~~~~~~~~~~~~~~~~~~~~~~~~~~~~~~~~~~~~~~~~~~~~~~~~~~~~~~~~~~~~~~~~~~~~~~~~~~
he3_multiplicity  no      # (yes/no) He3 module on/off
# ~~~~~~~~~~~~~~~~~~~~~~~~~~~~~~~~~~~~~~
# Select Capture Event Type
# ~~~~~~~~~~~~~~~~~~~~~~~~~~~~~~~~~~~~~~
output_sort_file    no   # (yes/no) Print out a file with all sorted events
```

Example Output File for MCNP – PoliMi Post Processing Code

```
Bin Values,     Total,      Neutrons,     Photons
    0.0010        0.0          0.0        0.0
   0.0020       337.0        337.0          0.0
   0.0030       301.0        301.0          0.0
   0.0040       257.0        257.0          0.0
   0.0050       235.0        235.0          0.0
   0.0060       180.0        180.0          0.0
   0.0070       149.0        149.0          0.0
   0.0080       144.0        144.0          0.0
   0.0090       121.0        121.0          0.0
   0.0100       129.0        129.0          0.0
    0.0110        90.0         90.0        0.0
    0.0120        78.0         78.0        0.0
    0.0130        83.0         83.0        0.0
    0.0140        66.0         66.0        0.0
    0.0150        61.0         61.0        0.0
    0.0160        50.0         50.0        0.0
```

0.0170	59.0	59.0	0.0
0.0180	56.0	56.0	0.0
0.0190	51.0	51.0	0.0
0.0200	49.0	49.0	0.0
0.0210	55.0	55.0	0.0
0.0220	39.0	39.0	0.0
0.0230	38.0	38.0	0.0
0.0240	36.0	36.0	0.0
0.0250	37.0	37.0	0.0
0.0260	38.0	38.0	0.0
0.0270	39.0	39.0	0.0
0.0280	32.0	32.0	0.0
0.0290	34.0	34.0	0.0
0.0300	22.0	22.0	0.0
0.0310	24.0	24.0	0.0
0.0320	24.0	24.0	0.0
0.0330	25.0	25.0	0.0
0.0340	22.0	22.0	0.0
0.0350	32.0	32.0	0.0
0.0360	26.0	26.0	0.0
0.0370	28.0	28.0	0.0
0.0380	22.0	22.0	0.0
0.0390	19.0	19.0	0.0
0.0400	34.0	34.0	0.0
0.0410	40.0	40.0	0.0
0.0420	24.0	24.0	0.0
0.0430	35.0	35.0	0.0
0.0440	35.0	35.0	0.0
0.0450	50.0	50.0	0.0
0.0460	53.0	53.0	0.0
0.0470	38.0	38.0	0.0
0.0480	46.0	46.0	0.0
0.0490	53.0	53.0	0.0
0.0500	53.0	53.0	0.0

…

…

…

11.9500	0.0	0.0	0.0
11.9510	0.0	0.0	0.0
11.9520	0.0	0.0	0.0
11.9530	0.0	0.0	0.0
11.9540	0.0	0.0	0.0
11.9550	0.0	0.0	0.0
11.9560	0.0	0.0	0.0
11.9570	0.0	0.0	0.0
11.9580	0.0	0.0	0.0
11.9590	0.0	0.0	0.0
11.9600	0.0	0.0	0.0
11.9610	0.0	0.0	0.0
11.9620	0.0	0.0	0.0
11.9630	0.0	0.0	0.0
11.9640	0.0	0.0	0.0
11.9650	0.0	0.0	0.0
11.9660	0.0	0.0	0.0
11.9670	0.0	0.0	0.0
11.9680	0.0	0.0	0.0
11.9690	0.0	0.0	0.0
11.9700	0.0	0.0	0.0
11.9710	0.0	0.0	0.0
11.9720	0.0	0.0	0.0
11.9730	0.0	0.0	0.0
11.9740	0.0	0.0	0.0
11.9750	0.0	0.0	0.0
11.9760	0.0	0.0	0.0
11.9770	0.0	0.0	0.0
11.9780	0.0	0.0	0.0
11.9790	0.0	0.0	0.0
11.9800	0.0	0.0	0.0
11.9810	0.0	0.0	0.0
11.9820	0.0	0.0	0.0
11.9830	0.0	0.0	0.0
11.9840	0.0	0.0	0.0

11.9850	0.0	0.0	0.0
11.9860	0.0	0.0	0.0
11.9870	0.0	0.0	0.0
11.9880	0.0	0.0	0.0
11.9890	0.0	0.0	0.0
11.9900	0.0	0.0	0.0
11.9910	0.0	0.0	0.0
11.9920	0.0	0.0	0.0
11.9930	0.0	0.0	0.0
11.9940	0.0	0.0	0.0
11.9950	0.0	0.0	0.0
11.9960	0.0	0.0	0.0
11.9970	0.0	0.0	0.0
11.9980	0.0	0.0	0.0
11.9990	0.0	0.0	0.0
12.0000	0.0	0.0	0.0

REFERENCES

[i] Knoll, Glenn, **Radiation Detection and Measurement** 3rd edition (2000).

[ii] Glasstone, S., Sesonske, A., **Nuclear Reactor Engineering** Van Nostrand Reinhold Company 1967 pg 92.

[iii] Thwaites, D., Tuohy, J., *Back to the Future: The History and Development of the Clinical Linear Accelerator*. **Physics in Medicine and Biology** 51 pg R343-R362 (2006).

[iv] TRI-CARB Liquid Scintillation Analyzer. Model 2000CA, Operation Manual. Publication No. 169-3029, Rev. D (1987).

[v] BURLE 8575 Photomultiplier Datasheet, BURLE INDUSTRIES, INC., 1989.

[vi] Brooks, F., *Development of Organic Scintillators*. **Nuc. Instr. Meth**. 162, 477-505 (1979).

[vii] Klein, H., Neumann, S., *Neutron and Photon Spectrometry with Liquid Scintillation Detectors. in Mixed Fields*. **Nuc. Instr. Meth**. 476, 132-142 (2002).

[viii] Verbinski, V., Burrus, W., *Calibration of an Organic Scintillator for Neutron Spectrometry*. **Nuc. Instr. Meth**. 65, 8-25 (1968).

[ix] Birks, John, **The Theory and Practice of Scintillation Counting** 2_{nd} edition (1964).

[x] Kuchnir, F., Lynch, F., *Time Dependence of Scintillators and the Effect on Pulse-Shape Discrimination***. IEEE Trans. On Nucl. Sci**. 15, 3, 107-113 (1968).

[xi] Bollinger, L., Thomas, G., *Measurement of the Time Dependence of Scintillation Intensity by a Delayed Coincidence Method*. **Rev. Sci. Instrum**. 32, 1044 (1961).

[xii] Carasco, C. *Organic Scintillators response function modeling for Monte Carlo Simulation of Time-of-Flight measurements.* **Appl Radiat Isot**. 70 (7):1367-9 (2012).

[xiii] Cross, W., Ing, H. Neutron Spectroscopy, The Dosimetry of Ionizing Radiation, Vol. II, Academic Press Inc. (1987).

[xiv] Reginatto, M. "The "Multi- Channel" Unfolding Programs in the UMG Package" MXD_MC33, GRV_MC33, and IQU_MC33 for UMG Package 3.3 released March 1st, 2004".

[xv] Matzke, M. *Unfolding Methods,* Physikalisch-Technische Bunesanstalt (PTB), D38116 Braunschweig, Germany.

[xvi] Bogart, D., et. al., *Transport Analysis of Measured Neutron Leakage Spectra from Spheres as Tests of Evaluated High-Energy Cross Sections*. **Nucl. Sci. Eng.** 53, 285-303 (1974).

[xvii] MCNPX – PoliMi Post-Processor (MPPost) Manual. Version 2.1.0 March 2012.

[xviii] Drosg, M. *Accurate Measurement of the Counting Efficiency of a NE-213 Neutron Detector Between 2 and 26 MeV*. **Nucl. Sci. Eng.** 105, 573-584 (1972).

[xix] Burrus, W., et. al., *Fast Neutron Spectroscopy with Thick Organic Scintillators*. **Nucl. Inst. Meth.** 67, 181-196 (1969).

[xx] Johnson, R., *Integral Tests of Neutron Cross Sections for Iron, Niobium, Beryllium, and Polyethylene,* Doctoral Thesis from University of Illinois at Urbana-Champaign, 1975.

[xxi] Cartegni, L. *Simulation of the Neutron Response Matrix for a Liquid Scintillator and Spectrum* Unfolding. ORNL/TM-2004/315. May 2005.

[xxii] SRIM Ion Stopping and Range Tables, James F. Ziegler, 2000.